L-subshell vacancy decay processes for elements with $52 \leq Z \leq 57$ following ionization using Mn $K\alpha$ x rays

Veena Sharma, Sanjeev Kumar, D. Mehta, and Nirmal Singh
Department of Physics, Panjab University, Chandigarh 160 014, India
(Received 16 January 2008; published 18 July 2008)

The L_i- ($i=1-3$) subshell x-ray spectra for the $_{52}$Te, $_{53}$I, $_{55}$Cs, $_{56}$Ba, and $_{57}$La elements excited by Mn $K\alpha$ ($E_{K\alpha_2}=5.888$ keV and $E_{K\alpha_1}=5.899$ keV) x rays have been investigated using the ^{55}Fe radioisotope in conjunction with a Cr absorber. A low-energy Ge detector was used to measure the L x rays at an emission angle $\psi=126°$, where the second-order Legendre polynomial term P_2 (cos ψ) associated with the angular distribution is annulled. In the case of the $_{56}$Ba and $_{57}$La elements, alignment of the L_3-subshell vacancy states was investigated through angular distribution measurements of the emitted L_3-subshell x rays. The $L\alpha_{1,2}$ and $L\beta_{2,15}$ x-ray groups are observed to be nearly isotropic, while the data for the pure Ll (L_3-M_1) x-ray emission are indicative of a small anisotropic trend, though within experimental error. The integral x-ray fluorescence cross sections are deduced and interpreted in terms of L_i-subshell photoionization cross sections, fluorescence and Coster-Kronig yields, and x-ray emission rates. The L_2-subshell x-ray cross sections for $_{57}$La measured using targets of lanthanum (III) fluoride and dilanthanum (III) trioxide are found to be unusually higher. The enhancement is observed due to the contribution of the L_2-subshell radiative resonant Raman scattering (RRS) of Mn $K\alpha$ x rays having energy around the L_2-subshell binding energy of $_{57}$La in these compounds. Also, the observed enhancement of the L_3-subshell x-ray cross sections in $_{57}$La is suggestive of intrashell vacancy transfer via L_2-L_3 Coster-Kronig RRS transitions. The L_2-subshell total RRS cross sections in $_{57}$La have been deduced from the present measured attenuation coefficients for Mn $K\alpha$ x rays in La_2O_3 and LaF_3. The L_2-subshell radiative and total RRS cross sections in $_{57}$La using LaF_3 are higher by $\sim$30% than those using La_2O_3. The contribution of processes predicted in the framework of Mozouchi's four-band model involving inner subshells along with the valence and conduction bands of these wide-band-gap insulator compounds is likely to account for the observed results. The L_2-subshell radiative and L_2-L_3 Coster-Kronig yields and the ratio of the L_2-M_4 and L_2-N_4 radiative RRS intensities in both La compounds are found to be same and are consistent with values from photoexcited vacancy decay. The L_2-subshell radiative RRS was also observed to be isotropic.

DOI: 10.1103/PhysRevA.78.012507 PACS number(s): 32.70.Jz, 32.30.Rj, 32.80.Fb, 32.50.+d

I. INTRODUCTION

The electron vacancy in an atomic L_i ($i=1-3$) subshell can be produced through direct ionization using photons or charged particles, electron-capture radioactive decay, internal-conversion decay, and during atomic deexcitation of K-shell vacancies. The L_i- ($i=1-3$) subshell vacancy states are characterized by total angular momentum values $J=\frac{1}{2}$, $\frac{1}{2}$, and $\frac{3}{2}$, respectively. The remnant ion rapidly relaxes in a very short time ($\sim 10^{-15}-10^{-16}$ s) by the characteristic x-ray emission, Auger transitions (intershell vacancy transfer), and Coster-Kronig (CK) transitions (intrashell vacancy transfer). Photoionization at energies away from the ionization threshold, being a better understood process, provides more reliable information regarding the number of primary L_i-subshell vacancies and hence is more appropriate to investigate the parameters related to various decay modes of the inner-shell vacancies. Photoionization methods offer substantial advantages in studying the inner-shell vacancy decay processes via fluorescent x-ray measurements due to precise energy tunability of the exciting photon beam, which provides selectivity in ionization among subshells of the target element. Furthermore, the complexities associated with multiple primary vacancies in different subshells are avoided. The L_i-subshell CK and fluorescence yields in medium- and high-Z elements have been deduced by measuring the L x rays emitted following selective ionization among the L_i subshells using tunable synchrotron sources [1,2], radioisotopes [3], an x-ray generator, and an energy-dispersive detection setup. Theoretical and experimental investigations in this direction have been thoroughly discussed in comprehensive review articles [4,5], and the results have been reassessed periodically and compiled [6–9]. Recently, a set of the fluorescence and CK yields for the elements with $25 \leq Z \leq 96$ has been recommended by Campbell [10]. Measurements of x-ray intensities using wavelength-dispersive detection equipment and an advanced tunable synchrotron source have gained impetus in recent times because of the opportunity to study individual x-ray, satellite, and hypersatellite lines [11,12]. The L_3 subshell with $J>\frac{1}{2}$ provides the least complex platform for investigating the alignment of ions by direct photoionization [13]. The inner-shell alignment can be inferred in the subsequent emission either via the degree of linear polarization of the fluorescent x rays or angular distribution of the fluorescent x rays or the Auger electron. Most of the experiments have been performed for the L_3-subshell ($J=\frac{3}{2}$) alignment through angular distribution measurements of the emitted x rays using experimental setups involving radioactive sources [14–16] and an x-ray generator [17]. Recently, measurements [18–20] using the polarized photon beam from a synchrotron source have also been performed. The measurements regarding anisotropy in L_3-subshell x-ray

emission following ionization by unpolarized photons requires precision experimental investigations.

Analogous to L_i-subshell real vacancy production through photoionization and its decay modes, the resonant Raman scattering (RRS) process involves virtual vacancy production and the associated decay modes. In case the incident photon energy approaches from below the L_i-subshell binding energy of the target element, the Raman scattering is resonantly enhanced. It proceeds by the creation of a L_i-subshell virtual hole with the corresponding electron excited in an unoccupied state; simultaneously, the core-hole states are relaxed by an electron transition from a higher shell. The electron transition results in a photon emission (radiative RRS) or an electron emission (Auger-CK decay) from the outer shell or subshell. Depending on the subshell in which a hole is created in the intermediate and final states, one observes different contributions to RRS similar to the fluorescent and Auger transitions. Sparks and Ice [21] and Manninen [22] have discussed different aspects of the RRS process along with its applications. Theoretical discussions regarding the radiative RRS process have been given by Tulkki and Åberg [23]. Most of the RRS measurements have been performed for radiative transitions using tunable synchrotron radiation sources (SRSs) and the wavelength-dispersive [24,25] and energy-dispersive [26] detection techniques. Recently, measurements have also been reported using the modest resolution energy-dispersive detection setups and photon sources based on radioisotopes [27] and those based on proton-induced x-ray emission (PIXE) [28]. A few measurements to investigate the angular dependence in K-shell radiative RRS emission [29,30] are also available. Brown *et al.* [31] identified the L_3-$M_{4,5}M_{4,5}$ Auger resonant Raman transitions for atomic $_{54}$Xe using monochromatized synchrotron radiation around the L_3-ionization threshold through observation of the resonance enhancement and linear dispersion of the Auger peaks as a function of incident photon energy. More efforts in this direction using high-resolution measurements led to observation of fine peak structure in the radiative [25] and Auger electron resonant Raman spectra [32,33]. The precision experimental data of the inner-shell binding energies in different chemical states of elements are important outcomes of such measurements [24]. Extensive efforts are required in studying the deexcitation processes associated with the virtual L_i-subshell vacancies, especially energy-sensitive intrashell vacancy transfer processes.

Analytical applications of the RRS process have also gained momentum during the past few years. The RRS cross sections are sensitive to the energy difference between the subshell ionization threshold and the incident photon beam energy and also to their energy widths. The RRS process enables us to perform spectroscopic studies on the chemical states, which directly reflect the bonding characters of the emitters in their specific environment. In the case of trace elemental analysis, the RRS can add to the complexity of the x-ray spectrum, e.g., difficulties due to the energetic degeneracy between the characteristic diagram lines of the trace element and the RRS of the matrix element. By incorporating contributions of the interfering radiative RRS to the x-ray fluorescence (XRF) spectra, a more precise description of the interelemental matrix effects will be possible and will lead to considerable improvements in x-ray-emission-based spectroscopic techniques. The RRS cross sections contribute significantly to the attenuation of x rays in matter especially at photon energies lower than the subshell electron binding energy (B_E) by less than $\sim 0.001 B_E$. The present available attenuation coefficients do not incorporate the contributions of RRS [34], which is otherwise difficult to estimate because of its considerable sensitivity to the physical and chemical states of atoms through the electron binding energy and band structure [28,35]. Precise theoretical understanding of the process is required.

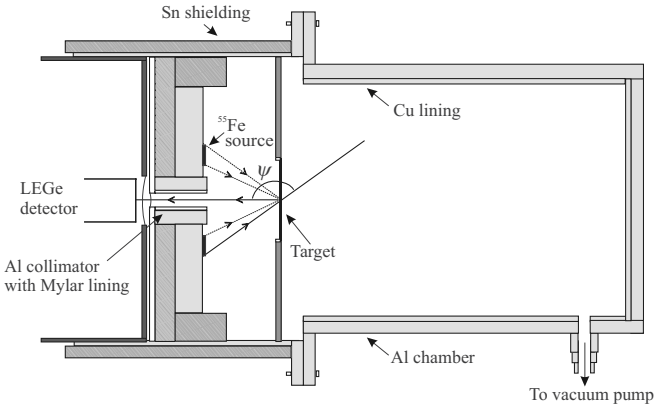

FIG. 1. Annular source, target, and detector geometrical arrangement used for the present L x-ray fluorescence measurements.

The present work probes the decay processes associated with the L_i-subshell vacancy states produced in the fluorescence and RRS processes, respectively. The investigations involve the L_i-subshell XRF differential cross section measurements for elements in the atomic region $52 \leq Z \leq 57$ using the Mn $K\alpha$ x rays. The observed enhanced intensity of the L_2-subshell x rays in the case of $_{57}$La is identified as a contribution of the L_2-subshell radiative RRS of the Mn K x rays. The fluorescence and RRS spectra are interpreted in terms of the fluorescence and CK transition probabilities associated with the corresponding process. Also, the angular dependences in L_3-subshell ($J=\frac{3}{2}$) fluorescent x-ray emission and L_2-subshell ($J=\frac{1}{2}$) radiative RRS have been investigated.

II. EXPERIMENTAL DETAILS

The source, target, and detector geometrical arrangement used for the present L_i-subshell XRF measurements is shown in Fig. 1. The Mn $K\alpha$ ($E_{K\alpha_2}=5.888$ keV, $E_{K\alpha_1}=5.899$ keV) x rays were obtained from an ^{55}Fe radioisotope annular source used in conjunction with a Cr absorber. The ^{55}Fe annular source (1.850 GBq, model IEC.A2, AEA Technology, Germany) is in the form of a circular flat ribbon of 34-mm diameter and 4-mm width. The ^{55}Fe radioisotope undergoes electron capture decay with $T_{1/2}=2.73$ years and results in emission of the Mn $K\alpha_2$, $K\alpha_1$, and $K\beta_1$ x rays with probabilities of 8.2, 16.2, and 2.86 per 100 decays [36], respectively. An annular foil of Cr ($B_K=5.9892$ keV [36]) was used with the ^{55}Fe source for selective absorption of the Mn $K\beta$ x rays ($E_{K\beta_1}=6.492$ keV). The values of the attenuation

TABLE I. Parameters related to the L_i $(i=1-3)$ subshells of the target elements used in the present measurements.

Element	Shell/ Subshell	Binding Energy (keV) [36]	Level width (eV) [37]	Photoionization cross sections (cm^2/g) [38] at energy of Mn$K\alpha_2$ x ray	Mn$K\alpha_1$ x ray	Fluorescence yield (ω_i) DHS [9] Campbell [10]	Barrea *et al.* [2,39]	Coster Kronig yield (f_{ij})	Campbell [10]	DHS [9]	Barrea *et al.* [2,39]
$_{52}$Te	L_1	4.9392	2.20	92	91	0.041		f_{12}	0.193	0.193	
								f_{13}	0.250	0.328	
	L_2	4.6120	2.84	139	138	0.078		f_{23}	0.153	0.172	
	L_3	4.3414	2.62	246	244	0.081					
	M,N,O			119	118						
$_{53}$I	L_1	5.1881	2.10	95	94	0.043		f_{12}	0.195	0.195	
								f_{13}	0.250	0.328	
	L_2	4.8521	2.95	151	150	0.084		f_{23}	0.156	0.173	
	L_3	4.5571	2.72	266	265	0.086					
	M,N,O			130	129						
$_{55}$Cs	L_1	5.7143	2.00	95	94	0.049		f_{12}	0.199	0.199	
								f_{13}	0.250	0.330	
	L_2	5.3594	3.15	164	163	0.097		f_{23}	0.159	0.177	
	L_3	5.0119	2.92	292	290	0.098					
	M,N,O			95	146						
$_{56}$Ba	L_1	5.9888	2.10	0	0	0.053	0.068(7)	f_{12}	0.201	0.201	0.156(2)
								f_{13}	0.250	0.331	0.296(3)
	L_2	5.6236	3.25	168	167	0.103	0.12(1)	f_{23}	0.159	0.178	0.189(1)
	L_3	5.2470	3.02	300	298	0.104	0.11(1)				
	M,N,O			155	154						
$_{57}$La [a]	L_1	6.2663	2.20	0	0	0.057	0.064(7)	f_{12}	0.201	0.201	0.212(20)
								f_{13}	0.250	0.328	0.358(30)
	L_2	5.8906	3.35	0	171	0.111	0.118(10)	f_{23}	0.159	0.176	0.174(10)
	L_3	5.4827	3.12	315	314	0.112	0.108(10)				
	M,N,O			158	157						

[a]As $E_{Ka2}(\mathrm{Mn}) < B_{L2}(\mathrm{La}) < E_{K\alpha1}(\mathrm{Mn})$, the La L_2 subshell will be ionized by the Mn $K\alpha_1$ x ray only.

coefficients for the Mn $K\alpha$ and $K\beta$ x rays in Cr are 68.6 and 423.5 cm^2/g [34], respectively. An intensity ratio $I_{K\beta}/I_{K\alpha}$ of better than 10^{-5} could be achieved using a Cr absorber of effective thickness ~25 mg/cm^2. The Cr absorbers were prepared by electrodepositing Cr on a Cu backing. As the Cr foil is brittle, a Mylar film was glued on the Cr side and the Cu backing was etched using dilute nitric acid. The purity of the Cr absorber was checked using the energy-dispersive x-ray fluorescence (EDXRF) setup involving a Mo-anode x-ray tube. Multiple Cr foils were used in front of the ^{55}Fe exciter source to ensure uniformity of the absorber. The source-target assembly was housed in an Al chamber lined inside with Cu. The chamber was equipped with a 4-mm collimator and a 2-μm Mylar window. The detection system consisted of a low-energy Ge (LEGe) detector (100 $mm^2 \times 10$ mm, 8-μm Be window, Canberra) in horizontal configuration and having an energy resolution [full width at half maximum (FWHM)] of ~150 eV for the Mn $K\alpha$ x rays. The detector was shielded using a Sn housing. The Al chamber with source-target assembly inside was mounted on the detector head. The x-ray spectra were collected using a PC-based multichannel analyzer (Multiport II, Canberra). The chamber was evacuated (~10^{-2} torr) to avoid attenuation of the low-energy x rays in the air and eliminate the K x-ray (E_{KX}=2.975 keV) peaks due to Ar present in the air. To achieve a highly reproducible geometry, the target-to-detector distance was adjusted for the maximum count rate of the target x rays. The count rate was observed to be constant within 1% over a distance of ~3 mm.

Spectroscopically pure thin foils of Te (100 and 194 $\mu g/cm^2$), RbI (47.8 $\mu g/cm^2$), CsBr (52.9 $\mu g/cm^2$), BaF_2 (52, 98, and 228 $\mu g/cm^2$), and LaF_3 (108, 193, and 288 $\mu g/cm^2$) on Mylar backing (thickness=3.5 and 6.3 μm) were used as L x-ray targets. These foils were procured from Micromatter, Deer Harbor, WA. The information regarding the free-atom L_i- $(i=1-3)$ subshell binding energy [36], level width [37], photoionization cross sections ($\sigma^P_{L_i}$) [38], and fluorescence (ω_i) and CK (f_{ij}) yields [9,10] of the target elements are given in Table I. The Mn $K\alpha$ x rays ionize the L_i $(i=1-3)$ subshells in the $_{52}$Te, $_{53}$I, and $_{55}$Cs atoms and the L_2 and L_3 subshells in the $_{56}$Ba atom. In the case of the $_{57}$La atom, the Mn $K\alpha_1$ x ray ionizes both the L_2

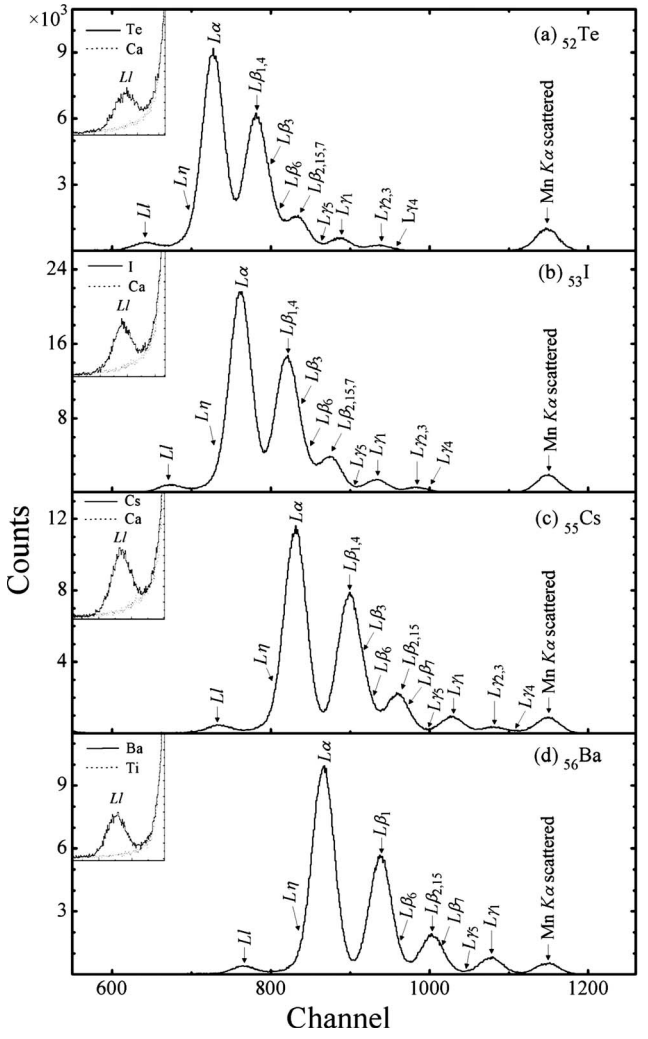

FIG. 2. Typical spectra of the L x rays from (a) Te, (b) NaI, (c) CsBr, and (d) BaF_2 targets excited by the Mn $K\alpha$ x rays from the ^{55}Fe source used in conjunction with the Cr absorber. Insets show the Ll x-ray peak area determination as mentioned in the text.

and L_3 subshells and the Mn $K\alpha_2$ x ray ionizes the L_3 subshell. Five spectra were taken using each target for a time duration in the range 5–15 h. The spectra were also taken in the same geometrical arrangement using a blank Mylar target to estimate the background. High-statistics measurements for weak components of the L x rays were also performed using thick targets ($\sim$200 mg/cm^2) of Te, NaI, $NaIO_3$, CsCl, $BaCO_3$, $Ba(NO_3)_2$, LaF_3, and La_2O_3 in pellet form. Typical L x ray spectra of the $_{52}$Te, $_{53}$I, $_{55}$Cs, $_{56}$Ba, and $_{57}$La elements are shown in Figs. 2(a)–2(d) and Figs. 3(a)–3(d), respectively. The recorded spectra exhibit peaks corresponding to the ionized L_i subshells along with the Mn $K\alpha$ x-ray elastic- and inelastic-scatter peaks. The intense x-ray components—viz., the Ll, $L\alpha_{1,2}$, $L\beta_6$, and $L\beta_{2,15,7}$ x rays from the L_3 subshell, the $L\eta$, $L\beta_1$, and $L\gamma_{1,5}$ x rays from the L_2 subshell, and the $L\beta_{3,4}$ and $L\gamma_{2,3,4}$ x rays from the L_1 subshell—are labeled in the spectra shown. Most of the L_i (i=1–3) subshell vacancies ($\sim$90%) decay through nonradiative transitions. The L_3-subshell x-ray intensity is enhanced due to transfer of $\sim$30% of the L_1-subshell vacancies and $\sim$15% of the L_2-subshell vacancies via the CK transitions.

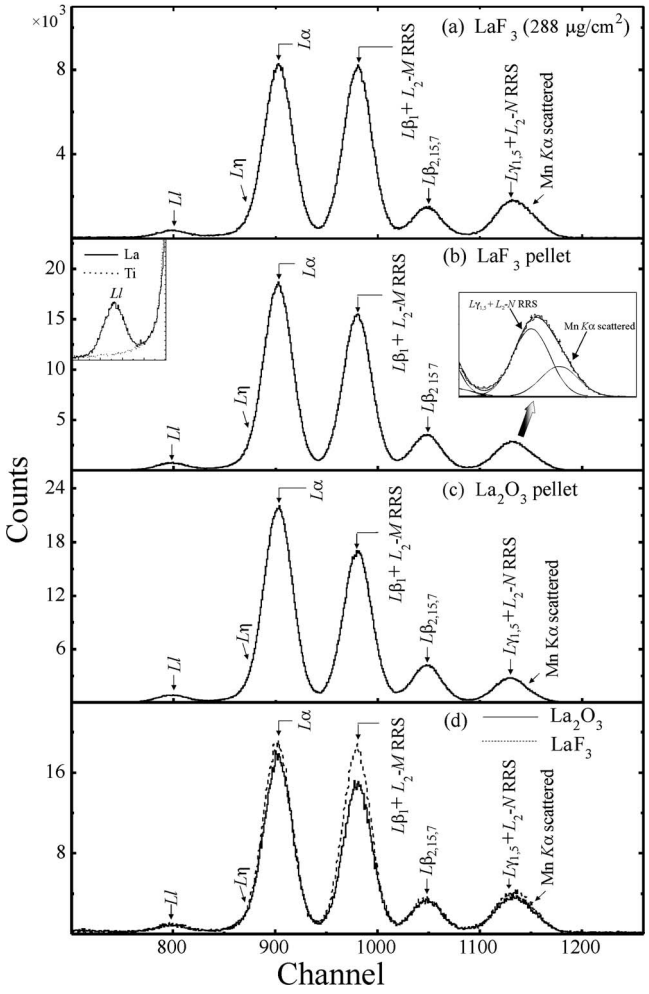

FIG. 3. Typical spectra of the L x rays from (a) the LaF_3 thin target, (b) the LaF_3 thick target, (c) the La_2O_3 thick target, and (d) the overlapped spectra from the LaF_3 and La_2O_3 thin targets excited by the Mn $K\alpha$ x rays from the ^{55}Fe exciter. The spectra in (d) are normalized for La mass thickness. Inset of (b) shows peak area determination for the Ll and $L\gamma_1$ x rays as mentioned in the text.

The K x-ray spectra from the Al (158 and 160.7 μg/cm^2), SiO (95 and 229 μg/cm^2), GaP (234 μg/cm^2), CuS (194 and 91.3 μg/cm^2), NaCl (46.5 and 48.7 μg/cm^2), KCl (44.3 μg/cm^2), CaF_2 (69 and 133 μg/cm^2), ScF_3 (104 and 199 μg/cm^2), Ti (78 and 112 μg/cm^2), and V (100.4 and 203 μg/cm^2) thin targets (Micromatter) were also taken in the same geometrical setup as used for the fluorescent L x-ray measurements. Spectra were also taken using NaCl, $CaCO_3$, and V_2O_5 pellets ($\sim$200 μg/cm^2) and Ti and V self-supporting foils. These spectra were used to determine the intensity of the exciting Mn $K\alpha$ x-ray photons and other geometrical factors as mentioned in Sec. III. The K x-ray spectra for the Ca and V targets taken at regular intervals were used to correct for the ^{55}Fe radioisotope decay during the measurements.

In the case of the annular source geometrical setup [Figs. 1 and 4(a)], the emission angle (ψ) for the x-ray photons reaching the detector could not be deduced from the energy difference between the elastic- and inelastic-scatter Mn $K\alpha$ x rays as the corresponding peaks were not resolved. The ef-

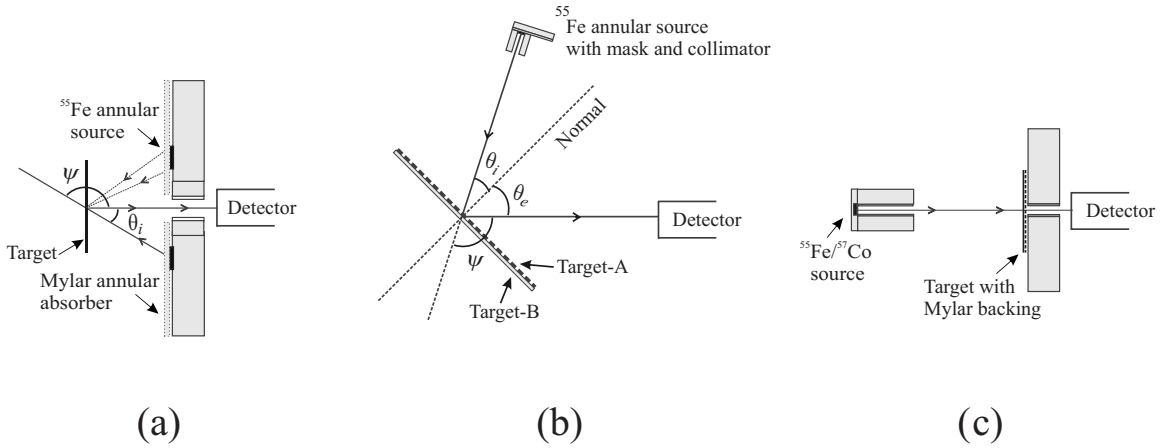

FIG. 4. (a) The schematic arrangement of the geometrical setup (Fig. 1) used for the *L* XRF cross section measurements, (b) the reflection geometrical arrangement involving the ^{55}Fe point source used for the angular distribution measurements, and (c) the transmission geometrical arrangement used for the attenuation measurements. Mylar annular absorber shown in (a) was placed for *in vivo* measurement of the incident angle (θ_i).

fective incident angle ($\theta_i = 180° - \psi$) between the incident beam and normal to the target surface was determined using an *in vivo* method based on attenuation of the Mn $K\alpha$ x rays. The *K* x-ray yields from the Ti and V targets were measured in vacuum with and without a Mylar annular absorber (10 mg/cm^2) placed in front of the ($J=\frac{1}{2}$)-Cr exciter as shown in Fig. 4(a). The effective incident angle (θ_i) was deduced from attenuation of the incident Mn *K* x rays in the Mylar absorber using the relation $I = I_0 \exp(-\mu x/\cos\,\theta_i)$. The product μx for the Mylar absorber was deduced by measuring the transmitted Mn *K* x rays in the geometrical arrangement shown in Fig. 4(c). The average emission angle for the annular source geometrical setup (Fig. 1) was found to be 126°. The reproducibility of the angle determination was verified using different *L* x-ray targets and Mylar absorbers.

In the present work, the angular dependence of the L_3-subshell x rays emitted following the $L_2(J=\frac{1}{2})$ and $L_3(J=\frac{3}{2})$ subshell photoionization in the case of $_{56}$Ba and $_{57}$La and L_2-subshell ($J=\frac{1}{2}$) radiative RRS in the case of $_{57}$La were also measured. These measurements are required to infer alignment of the L_i-subshell vacancy states produced in the photoionization and RRS processes and also to deduce the integral cross sections. The schematic arrangement of the geometrical setup [40] used for the angular distribution measurements is shown in Fig. 4(b). It involves a photon point source and a detector in the horizontal plane with the target placed at the center. The emission angle for the angular distribution measurements was changed by rotating the source about the central axis. The target was kept fixed in the vertical position at the center, making a 45° angle with the detector axis. The ^{55}Fe annular source equipped with a 20-mg/cm^2 Cr absorber was converted to a point source using a Cu mask and a 5-mm collimator. The source-target assembly was kept inside an Al chamber lined with Cu. The chamber was equipped with a collimator (diameter=3 mm, length=25 mm) and a 2-μm Mylar window. The LEGe detector was kept outside the chamber in air at a distance of ~2 mm. Spectroscopically pure targets of $BaCO_3$ and LaF_3 in pellet form (~200 mg/cm^2) were used for the angular distribution measurements. The isotropic emitted Ba $L\beta_1$ x ray originating from the $L_2(J=\frac{1}{2})$ subshell was used for normalizing the L_3-subshell x rays measured at different emission angles. A CaF_2 thin target (133 μg/cm^2) with a 6.3-μm Mylar backing was placed in conjunction with the LaF_3 thick target, and the isotropically emitted Ca *K*-shell ($J=\frac{1}{2}$) x rays were measured simultaneously. The uniformity of the CaF_2 reference target was verified to be better than 2% by the x-ray attenuation method [Fig. 4(c)]. The angle scans were performed manually in the horizontal plane ($\phi=0°$) by rotating the source arm over the angular range of $\psi=90°-160°$ for time durations of 50 h at each angle. The Ca $K\alpha$ x-ray yield measured simultaneously at different emission angles was used for normalizing the measured yields of the $L\alpha$, $L\beta_1$, and $L\beta_{2,15}$ x rays of the $_{57}$La element. The Ca $K\beta$ x-ray peak overlaps with the La Ll x-ray peak. A second set of spectra were taken to measure angular distribution of the Ll x rays without using the CaF_2 reference target. The main advantage of the present setup and procedure over earlier measurements [14–17] is that the target-detector geometry was not disturbed. The details and other advantages of the present geometrical setup and procedure have been discussed elsewhere [40].

III. EVALUATION PROCEDURE

The differential cross sections for the *q*th group of L_i-subshell fluorescent x rays in the $_{52}$Te, $_{53}$I, $_{55}$Cs, and $_{56}$Ba elements at the Mn $K\alpha$ x-ray excitation energy have been evaluated using the expression

$$\frac{d\sigma_{Lq}}{d\Omega}(\psi) = \frac{N_{Lq}}{m_u \beta_{Lq} (I_0 G)_{K\alpha} \varepsilon_{Lq}}, \tag{1}$$

where N_{Lq} is the photopeak area per unit time corresponding to the *q*th group of L_i-subshell x rays of the *u*th element of interest in the compound target, $(I_0 G)_{K\alpha}$ is the intensity of the exciting radiation falling on area of the target visible to the detector, ε_{Lq} is the detector efficiency at the Lq x-ray

energy, m_u is the mass-thickness of the uth element in the target foil in g/cm^2, and β_{Lq} is the self-absorption correction factor that accounts for attenuation of the incident Mn $K\alpha$ x rays and the emitted Lq x rays in the target. The values of β_{Lq} have been calculated using the expression

$$\beta_{Lq} = \frac{1 - \exp\left[-\sum_s (\mu_1^s/\cos\,\theta_i + \mu_{2q}^s/\cos\,\theta_e)m_s\right]}{\sum_s (\mu_1^s/\cos\,\theta_i + \mu_{2q}^s/\cos\,\theta_e)m_s}, \quad (2)$$

where s stands for different elements present in the target. θ_i is the angle of incidence for the incident Mn $K\alpha$ x rays, and θ_e is the angle of emission for the Lq x rays with respect to normal to the target. μ_1^s and μ_{2q}^s are the mass-attenuation coefficients for the incident Mn $K\alpha$ x rays and the emitted Lq x rays of uth element of interest present in the target and were taken from tables of Berger and Hubbell [34]. The values of β_{Lq} are ~0.95 for thin targets and <0.21 for thick targets used in the present work. The targets in pellet form behave like infinitely thick targets, i.e., having thickness more than a value that can provide 99% of the maximum count rate for the emitted fluorescent x rays. A value of β equal to 0.21 corresponds to 99% attenuation, and below this value of β, the effective thickness of the uth element in the multielement target can safely be taken as a constant equal to the limiting value of the $m\beta$ factor when $m \to \infty$, i.e.,

$$m_u\beta_{Lq} = w_u\left[\sum_s \{\mu_1^s/\cos\,\theta_i + \mu_{2q}^s/\cos\,\theta_e\}\right]^{-1}, \quad (3)$$

where w_u represents the weight fraction of the uth element in the multielemental target. The effective thickness $m\beta$ [Eq. (3)], especially in the case of thick targets, depends upon the photon incident (θ_i) and emission (θ_e) angles. The distribution of the θ_i, θ_e, and ψ angles in the geometrical setup determined using computer simulations is shown in Fig. 5(c). The effect of angular spread [Fig. 5(c)] on the $m\beta$ parameter is verified as mentioned in Appendix A.

Each spectrum was analyzed for the L x-ray photopeak areas using the computer code PEAKFIT [41]. It involves a nonlinear least-squares fitting routine involving fitting of multi-Gaussian functions plus a polynomial background. The peak fitting procedure consisted of two steps. In the first step, fitting was done for the $K\alpha$ x-ray peaks of the Al, Si, P, S, Cl, Ca, Ti, V, Mn, and Fe elements by allowing the FWHM to vary. The spectra for the Mn and Fe K x rays were taken using ^{55}Fe and ^{57}Co radioactive sources. The $K\alpha$ x-ray peak consists of the $K\alpha_1$ and $K\alpha_2$ x-ray components with intensity ratio of ~2 and the energy difference increasing from 1 eV for Si to 8 eV in case of V, and it can be taken as monochromatic for FWHM determination. This was confirmed by peak analysis of a simulated $K\alpha$ x-ray spectrum consisting of two x-ray components with an intensity ratio of ~2 and differing in energy by 10 eV. The change in FWHM was observed to be not significant (<1 eV). A plot of the FWHM as a function of energy is shown in Fig. 5(b), and it exhibits a small variation over the energy region of interest. In the second step, different L x ray peaks were fitted by fixing the FWHM to the interpolated values and centroids of weak peaks to

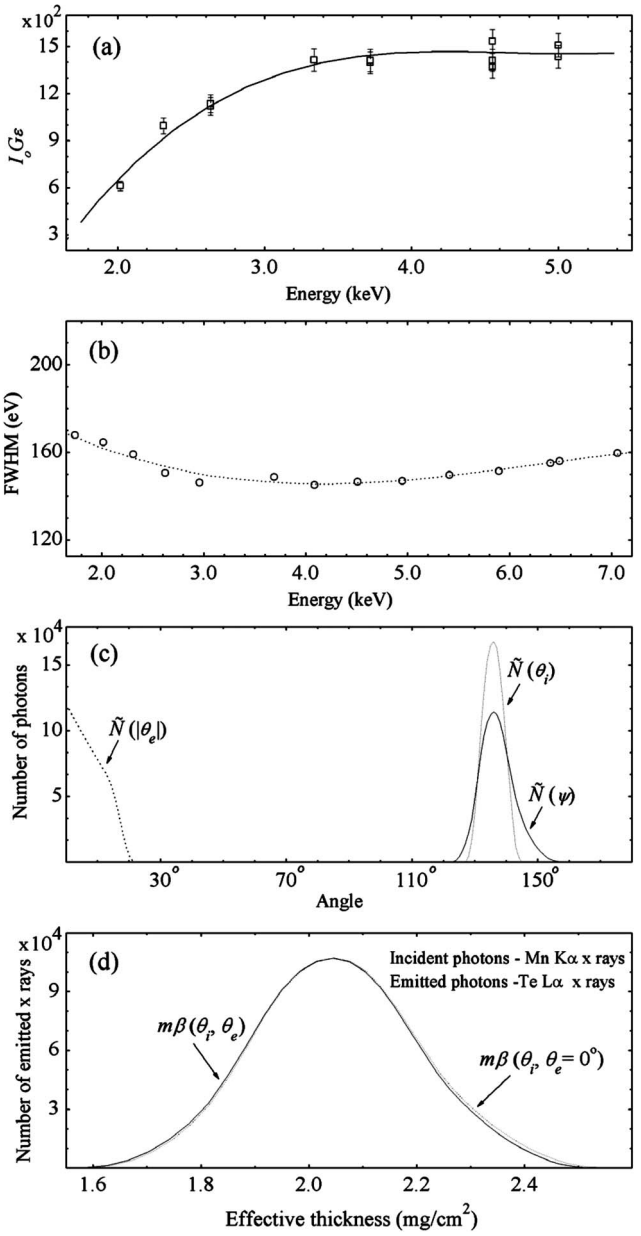

FIG. 5. (a) The product $I_0 G\varepsilon$ and (b) FWHM for the LEGe detector used in the geometrical setup (Fig. 1) as a function of detected photon energy. (c) The distribution of the θ_i, θ_e, and ψ angles in the present annular source geometrical setup and (d) the corresponding distribution of effective thickness [$m\beta(\theta_i, \theta_e)$] of the Te thick target for the $L\alpha$ x-ray emission.

their known energies [36]. The relative peak areas for the close-lying peaks varied significantly with FWHM, but the total area remained the same. In such cases, the cross sections have been evaluated for the group; e.g., the L_η and $L\beta_{3,4}$ x-ray peak areas have been added to the $L\alpha$ and $L\beta_1$ x-ray peak areas, respectively. The FWHM for the intrinsic Lorentzian broadening associated with the L x-ray lines is less than 12 eV [37,42] and is small as compared to ~150 eV for the Gaussian response function of the LEGe detector in the energy region of interest. The peak areas for the quoted L x-ray groups were found to be consistent even with a variation of 5% in the FWHM. The weak Ll x-ray

peak lies on the lower tail of the intense $L\alpha$ x-ray peak. The smoothly varying tail of the $L\alpha$ x-ray peak under the Ll x-ray peak can lead to significant error in the Ll x-ray peak area evaluation using the fitting procedure. For the Ll x-ray peak area evaluation, the lower-energy tail portion of the $K\alpha$ x-ray peak of the Ti or Ca element after the background subtraction was grafted to the $L\alpha$ x-ray peak to deduce the background beneath the Ll x-ray peak [inset of Figs. 2(a)–2(d) and Fig. 3(b)]. The net total counts over the clean peak region (within the $\pm 2\sigma$ region about the centroid) after background subtraction were used for normalization of the $K\alpha$ x-ray peak area with that of the $L\alpha$ x-ray peak. The results obtained by choosing different regions for the normalization were found to be consistent. The energy difference between the $L\alpha_1$ and $L\alpha_2$ x-ray components [intensity ratio $(I_{L\alpha_1}/I_{L\alpha_2}) \sim 9$] and between the $K\alpha_1$ and $K\alpha_2$ x-ray peaks of Ti and Ca is only few eV. The observed L x-ray spectra were also corrected for small contributions ($<1\%$) from decay of the L_i-subshell and K-shell vacancies produced by the bremsstrahlung from the ^{55}Fe source. The K x-ray peaks due to excitation by bremsstrahlung were also observed in the spectra of thick targets and were used for estimating these corrections [3]. In measurements using thick elemental targets, the enhancement of the L_3-subshell x rays due to additional ionization by the target $L\gamma_1$ x ray with energies above the L_3-subshell binding energy (B_{L_3}) was estimated to be $\sim 2\%$. This estimation has been done by comparing the $L\alpha$ and $L\beta_1$ x ray intensity ratios measured using the thick and thin Te targets. In the case of thick targets for other elements prepared using their compounds, such an enhancement is diluted by the presence of other elements. The enhancement correction is negligible for thin targets. Significant enhancement of $\sim 8\%$ has been observed [3] in the case of the L_i- ($i=1-3$) subshell excitation of a $_{92}$U thick target due to excitation by emitted $L\beta_{1,3}$ and $L\gamma$ x rays having energies above B_{L_3}.

The $(I_0G)_{K\alpha}\varepsilon_{Lq}$ values over the energy region 1.5–5.0 keV were deduced from the measured K x-ray yields of the Al, Si, P, S, Cl, Ca, Ti, and V elements from Al, SiO, GaP, CuS, NaCl and KCl, CaF_2, ScF_3, Ti, and V targets, respectively. The expression for $(I_0G)_{K\alpha}\varepsilon_{Lq}$ is given by

$$(I_0G)_{K\alpha}\varepsilon_{KX} = \frac{4\pi N_{KX}}{\sigma_{KX}\beta_{KX}m}, \tag{4}$$

where all symbols have the same meaning as in Eq. (1) and correspond to the K x rays. The K XRF cross sections were taken from the tables of Puri *et al.* [43]. Figure 5(a) shows a plot of the product $(I_0G)_{K\alpha}\varepsilon_{KX}$ as a function of the detected photon energy. The thickness of the thin foils was verified by the Mn K x-ray attenuation method in the transmission geometry [Fig. 4(c)] and necessary corrections in thickness of the targets were applied wherever necessary. This led to improvement in the efficiency values, and the error in the efficiency calibration is estimated to be $\sim 3\%$ over the energy region of interest. The same procedure was also used to confirm the quoted thickness of the L x-ray thin targets.

For the $_{52}$Te, $_{55}$Cs, and $_{56}$Ba elements, the incident photon beam from the source can be safely considered as a quasimonochromatic source of 5.895 keV, which is the weighted average energy of the $K\alpha_1$ and $K\alpha_2$ x rays taken after correcting the intensity for self-absorption. In the case of the $_{57}$La element, the L_2 subshell is ionized only by the $K\alpha_1$ x-ray component, whereas the L_3 subshell is ionized by both the $K\alpha_1$ and $K\alpha_2$ x rays. The intensity values of the incident $K\alpha_1$ and $K\alpha_2$ x rays, $(I_oG)_{K\lambda}$ ($\lambda=\alpha_1$ and α_2), were deduced using the expression

$$(I_0G)_{K\lambda} = \frac{N_{K\alpha}}{\left[\frac{(I_0G)_{K\alpha_2}}{(I_0G)_{K\lambda}}\beta_{K\alpha}^{K\alpha_2}\sigma_{K\alpha}^{K\alpha_2} + \frac{(I_0G)_{K\alpha_1}}{(I_0G)_{K\lambda}}\beta_{K\alpha}^{K\alpha_1}\sigma_{K\alpha}^{K\alpha_1}\right] m\varepsilon_{K\alpha}}, \tag{5}$$

where various symbols have the same meaning as mentioned earlier. However, the superscript of β corresponds to a component of the Mn $K\alpha$ x ray available for excitation. The intensity ratio of the $K\alpha_1$ and $K\alpha_2$ x rays was deduced to be 1.981 using the value taken from [36] after correcting $\sim 0.7\%$ for absorption in the Cr absorber and self-absorption in the ^{55}Fe source. The self-absorption thickness was deduced to be ~ 4 mg/cm^2 from the ratio of the Mn $K\beta$ and $K\alpha$ x-ray intensities measured under vacuum from the ^{55}Fe exciter source placed at different angles in front of the detector.

In the present angular-dependence measurements in case of the L_3-subshell x rays (or L_2-subshell RRS), anisotropy can be inferred from the ratio of the corresponding differential cross sections to that of the L_2-subshell ($J=\frac{1}{2}$) x ray of the same element or the K shell ($J=\frac{1}{2}$) x-ray of the Ca reference target. The ratio of differential cross sections, $R(\psi)$, at different emission angles is calculated using the equation

$$R(\psi) = \wp\frac{N_{L_3}\beta_{K(L_2)}\tau_{\text{in}}}{N_{K(L_2)}\beta_{L_3}}, \tag{6}$$

where τ_{in} is the attenuation correction for the incident photons in the reference target, if any. N_{L_3} and $N_{K(L_2)}$ are the simultaneously measured yields of the L_3-subshell x rays (or L_2-subshell RRS) and the reference K-shell (or L_2-subshell) x rays, respectively. The term $\wp$ is the product of the attenuation correction of the emitted x rays in the reference target, the ratio of the mass thickness of the targets and the $\varepsilon_L/\varepsilon_K$ factor. The value of the term $\wp$ remains constant at different angles as the target-detector geometry was not disturbed. The I_oG factor cancels out as the L and K x rays have been measured simultaneously. The angular dependence of the β and τ parameters on the angle of incidence is considerably reduced in the present geometrical setups as θ_e is fixed and θ_i varies over half the angular range of emission angles in each quadrant. The absorption-correction factors (β) for the LaF_3 target corresponding to the emitted L_2- and L_3-subshell x rays of $_{57}$La and their ratios are plotted as a function of emission angle in Figs. 6(a) and 6(b), respectively. Thus anisotropy of the Lq x rays is mainly dependent on the peak area ratio N_{Lq}/N_K measured at different angles. The peak areas for the angular-dependence investigations, N_{Lq} and N_K, were taken as the total net counts over the peak region after subtracting the linear background extrapolated from the ob-

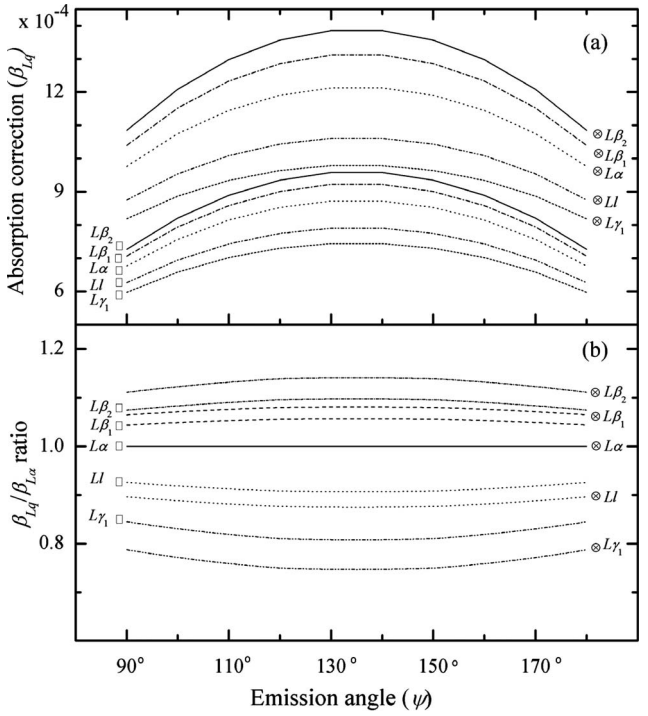

FIG. 6. (a) The absorption correction factors (β_{Lq}) for the emitted Ll, $L\alpha$, $L\beta_1$, $L\beta_2$, and $L\gamma_1$ x rays of $_{57}$La in the LaF_3 target and (b) their ratios with that for the $L\alpha$ x rays are plotted as a function of emission angle. ⊗ and □ correspond to excitation by the Mn $K\alpha_1$ and $K\alpha_2$ x rays, respectively.

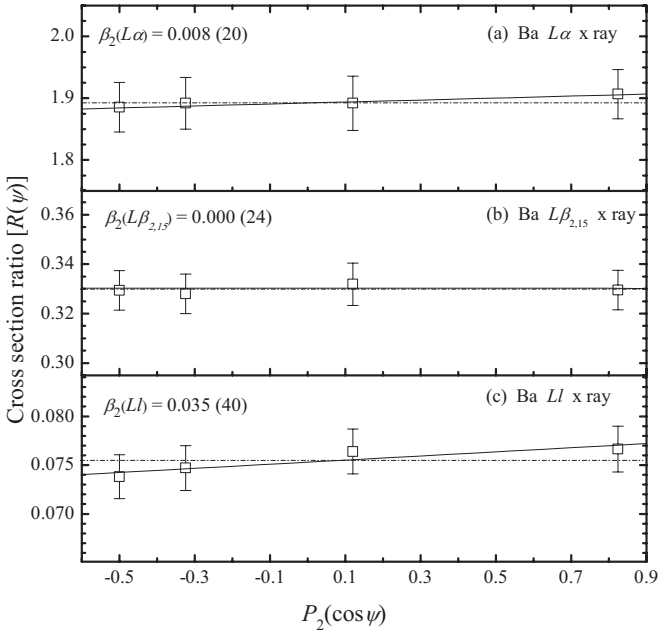

FIG. 7. The cross section ratios $R(\psi)$ for the (a) Ll, (b) $L\alpha$, and (c) $L\beta_{2,15}$ x rays with respect to the isotropically emitted $L\beta_1$ x ray in the case of $_{56}$Ba as a function of $P_2(\cos\psi)$. The β_2 value for the Ll x ray is corrected for contribution of the $L\alpha$ x rays.

served spectra. The peak-fitting procedure was not used to avoid fitting error.

IV. RESULTS AND DISCUSSION

A. Alignment of L_3-subshell vacancies in $_{56}$Ba and $_{57}$La

The angular distribution of the L_3-subshell fluorescent radiations emitted following ionization by the unpolarized photons is represented by $I(\psi)=I_0[1+\beta_2 P_2(\cos\psi)]$, where $P_2(\cos\psi)$ is the second-order Legendre polynomial and β_2 is the coefficient of anisotropy [13]. In the present measurements in the case of $_{56}$Ba, the anisotropy parameter $R(\psi)$ was deduced using Eq. (6) for the Ll, $L\alpha$, and $L\beta_{2,15}$ x rays with the isotropically emitted $L\beta_1$ x ray originating from the L_2 subshell ($J=\frac{1}{2}$) taken as the reference. The $L\beta_1$ x ray also contains a small contribution ~2% of the L_3-subshell x rays. Uncertainty in the $R(\psi)$ parameter is ≤3%, which is mainly due to the statistical error and precariousness associated with peak area determination, especially for the Ll x-ray peak. The Ll x-ray peak area was deduced by linearly extrapolating the nearly constant background from its left. The deduced peak area included about 20% contribution from the $L\alpha$ x-ray peak. This contribution was estimated by comparing the Ll x-ray peak area determined by this method with that using the peak-grafting procedure mentioned in Sec. III. It will dilute the observed anisotropy in the Ll x-ray emission as the angular dependence of the $L\alpha$ x rays is observed to be not significant and has been taken as a correction factor. Such a method of peak area determination was preferred to avoid error due to separation of peaks using different procedures. The plots of the $R(\psi)$ parameter for the Ll, $L\alpha$, and $L\beta_{2,15}$ x rays as a function of $P_2(\cos\psi)$ are shown in Figs. 7(a)–7(c). In the case of $_{57}$La, the L_3-subshell x rays are produced by the Mn $K\alpha_1$ and $K\alpha_2$ x rays having widely differing attenuation coefficients in the target. A special evaluation procedure given in Appendix B was used to investigate the anisotropy. The differential cross sections for the $L\alpha$ and $L\beta_{2,15}$ x rays were measured relative to the isotropically emitted Ca K x rays from the CaF_2 reference target. For the Ll x-ray emission, the anisotropy is deduced relative to that of the $L\alpha$ x rays. The $L\alpha$, $L\beta_{2,15}$, and Ll x-ray fluorescence differential cross sections are plotted in Figs. 8(a), 8(c), and 8(d), respectively. The plots for the $L\alpha$ and $L\beta_{2,15}$ x rays in $_{56}$Ba [Figs. 7(b) and 7(c)] and $_{57}$La clearly evince isotropy. The plots for the Ll x ray [Figs. 7(a) and 8(d)] exhibit a small increasing trend in $R(\psi)$ though within experimental error (≤3%).

The anisotropy coefficient is expressed as $\beta_2=a\kappa A_{20}$, where A_{20} is the degree of alignment and the coefficient α depends only on the angular momentum of the initial and final states of the ionized atom. κ is the correction factor due to vacancy transfer via the CK transition. Berezhko, Kabachnik, and Rostovsky [44] have calculated the A_{20} coefficients for photoionization in the L_3 subshell of the $_{56}$Ba atom using the wave functions obtained in the Herman-Skilman (HS) potential. The A_{20} coefficient for the L_3 subshell decreases rapidly at the photon energies in the vicinity of the ionization threshold and remains constant at 0.11 at photon energies a few eV above the L_3-subshell ionization threshold. The incident photon energy is a few hundred eV above the L_3 ($J=\frac{3}{2}$) subshell binding energy in the case of $_{56}$Ba and $_{57}$La. The value of α has been calculated theoretically using the

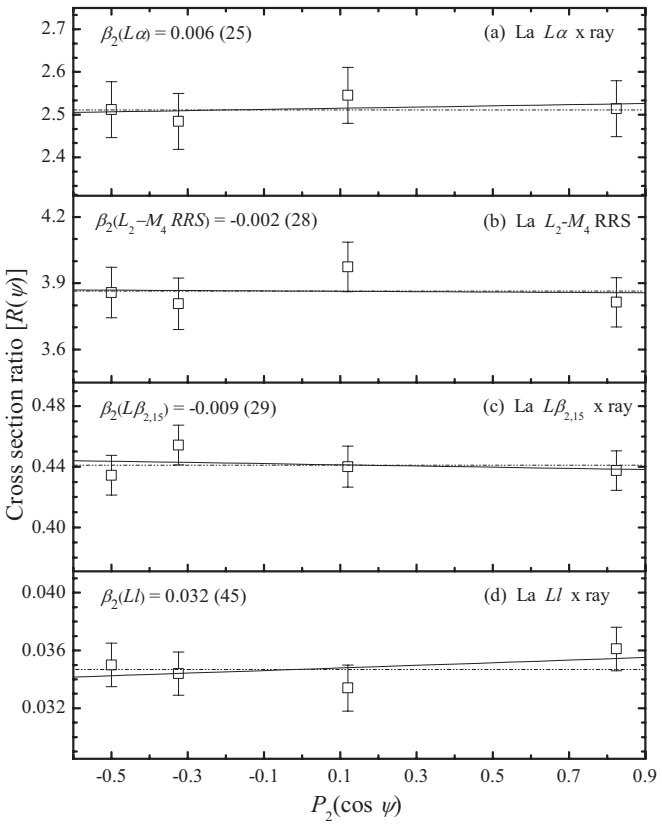

FIG. 8. The cross section ratio $R(\psi)$ for (a) $L\alpha$, (b) L_2-M_4 RRS, (c) $L\beta_{2,15}$, and (d) Ll x rays in the LaF_3 target as a function of $P_2(\cos\ \psi)$. The ratios in (a), (b), and (c) are with respect to the isotropically emitted Ca *K*-shell ($J=\frac{1}{2}$) x rays and in (d) are relative to the $L\alpha$ x rays.

single-particle model [45] as $\alpha(Ll)=0.5$, $\langle\alpha(L\alpha)\rangle=0.05$ [$\alpha(L\alpha_2)=-0.4$ and $\alpha(L\alpha_1)=0.1$], and $\langle\alpha(L\beta_{2,15})\rangle=0.044$; where the average $\langle\alpha\rangle$ values have been evaluated using intensity as the weighing factor. κ_{L_3} is given by $\kappa_{L_3}=\sigma^P_{L_3}(\sigma^P_{L_3}+f_{23}\sigma^P_{L_2})^{-1}$. Its value is calculated to be ~0.91 for $_{56}$Ba using the f_{23} value recommended by Campbell [10] and the $\sigma^P_{L_i}$ values obtained by a relativistic treatment of the ionization process and employing the relativistic Hatree-Slater potential [38]. The value of κ_{L_3} is deduced to be 0.97 for $_{57}$La by taking into account the relative intensities of the incident Mn $K\alpha_1$ and $K\alpha_2$ x rays. Theoretically predicted $A_{20}\sim 0.11$ [44] corresponds to the intensity ratios $[I(90°)/I(160°)]$ ~0.94 for the Ll x ray and >0.99 for the $L\alpha$ and $L\beta_{2,15}$ x rays. Despite the relatively large error associated with $R(\psi)$ for the L_3-subshell x rays, the hypothesis of anisotropy was attempted in light of its small predicted magnitude.

The β_2 coefficients obtained by fitting the angular-distribution polynomial are $\beta_2(Ll)=0.035(40)$, $\beta_2(L\alpha)=0.008(20)$, and $\beta_2(L\beta_{2,15})=0.000(24)$ [Figs. 7(a)–7(c)] for $_{56}$Ba, and $\beta_2(Ll)=0.038(51)$, $\beta_2(L\alpha)=0.006(25)$, and $\beta_2(L\beta_{2,15})=-0.009(29)$ for $_{57}$La. The $\beta_2(Ll)$ has been corrected for the isotropic contribution ~20% of the $L\alpha$ x-ray peak area as mentioned earlier in this section. The $\beta_2(Ll)$ value in the case of $_{57}$La has been corrected for the observed anisotropy $[\beta_2(L\alpha)=0.006(25)]$ in the $L\alpha$ x-ray emission. This indicates that the observed emission of the *La* and $L\beta_{2,15}$ groups of x rays from $_{56}$Ba and $_{57}$La is nearly isotropic, which are also expected in view of the small $\langle\alpha(L\alpha)\rangle=0.05$ and $\langle\alpha(L\beta_{2,15})\rangle=0.044$ values due to opposite signs of the α coefficients for the unresolved x-ray components in these groups as mentioned above. The A_{20} value for the L_3 subshell deduced from the $\beta_2(Ll)$ is ~0.08(9) and ~0.08(11) in $_{56}$Ba and $_{57}$La, respectively, which are of the order of the theoretically predicted value ~0.11 [44].

The present measurements with a special procedure to minimize systematic errors conclude that emission of the $L\alpha_{1,2}$, and $L\beta_{2,15}$ fluorescent x-ray groups is observed to be nearly isotropic. The pure Ll x-ray emission from the L_3 subshell exhibits a small anisotropic trend. Further experimental precision needs to be improved to provide data to verify the theoretical predictions. It is worth mentioning that the experimental investigations for the high-*Z* elements reported by different groups [14–18] exhibit contradictory observations. Two groups [14,15] have claimed strong anisotropy in emission of L_3-subshell x rays for elements with $70\leq Z\leq 92$ while other groups have reported that L_3-subshell x-ray emission is isotropic within experimental error [16] or associated with small anisotropy [17–20]. The present measurements using a better experimental setup and procedure [40] clearly support the observations by the latter groups. Detailed comments on the investigations reporting unusually large anisotropy have already been included elsewhere [16,40].

B. X-ray fluorescence cross sections

In the present work, the *L* x-ray emission is observed to be isotropic and also the differential cross sections have been measured at 126° emission angle using annular source geometry, where the second-order Legendre polynomial term $P_2(\cos\ \psi)\sim 0$. The integral *L* XRF cross sections were deduced by multiplying the differential ones by a factor of 4π and are given in Table II. The percentage error in the measured cross sections is estimated to be 4%–6% and is attributed to uncertainties in the different parameters used in Eq. (1)namely, errors in mass thickness of the target, photopeak area evaluation (~4% for the Ll x-ray peak and ~2% for the other peaks), and the attenuation coefficients used to evaluate β (~4%) and the $I_oG\varepsilon$ factor (~3%). The error in thickness of thin targets with Mylar backing is 3%. In the thick targets, the error in the product, $m\beta$, is due to attenuation coefficients. The cross sections for different elements measured using thin and thick targets are found to agree within experimental error and their weighted average is given in Table II.

The present measured XRF cross sections are also compared with those calculated using L_i-subshell photoionization cross sections, fluorescence and CK yields, and x-ray emission rates in the equation

$$\sigma_{Lq}=\sigma^{P\tau}_{L_i}\omega_i F_{iq}, \tag{7}$$

where $\sigma^{P\tau}_{L_i}$ is the total number of vacancies in the L_i subshell including those transferred through CK transitions and is given by $\sigma^{P\tau}_{L_i}=\sigma^P_{L_i}+\Sigma_{j<i}\sigma^{P\tau}_{L_j}f_{ji}$. The $\sigma^P_{L_i}$ have been taken from

TABLE II. Integral L_i subshell XRF cross sections in $_{52}$Te, $_{53}$I, $_{55}$Cs, $_{56}$Ba, and $_{57}$La.

			L x-ray fluorescence cross-sections (cm^2/g)				
				Calculated			
Element	Fluorescence transition (subshell)	Transition energy (keV)	Experimental	σ_{Lq} (Campbell-DF)	σ_{Lq} (Campbell-DHS)	σ_{Lq} (Chen-DF)	σ_{Lq} (Barrea)
$_{52}$Te	$Ll(L_3)$	3.231	0.86(5)	0.78	0.795	0.805	
	$L\alpha(L_3),L\eta(L_2)$	3.766	20.1(9)	20.1	20.3	20.8	
	$L\beta_{1,3,4,6}(L_2,L_1,L_1,L_3)$	4.046	13.5(6)	13.5	13.6	13.5	
	$L\beta_{2,15,7}(L_3),L\gamma_5(L_2)$	4.302	2.70(12)	2.93	2.73	3.03	
	$L\gamma_1(L_2)$	4.567	1.48(6)	1.55	1.43	1.55	
	$L\gamma_{2,3}(L_1)$	4.826	0.658(30)	0.653	0.632	0.653	
	$L\gamma_4(L_1)$	4.934	0.051(3)	0.051	0.038	0.051	
$_{53}$I	$Ll(L_3)$	3.381	0.93(5)	0.89	0.911	0.920	
	$L\alpha(L_3),L\eta(L_2)$	3.934	22.0(9)	22.9	23.20	23.7	
	$L\beta_{1,3,4,6}(L_2,L_1,L_1,L_3)$	4.236	14.9(6)	15.3	15.453	15.3	
	$L\beta_{2,15,7}(L_3),L\gamma_5(L_2)$	4.508	3.33(15)	3.49	3.244	3.61	
	$L\gamma_1(L_2)$	4.793	1.68(7)	1.87	1.757	1.87	
	$L\gamma_{2,3}(L_1)$	5.059	0.670(30)	0.719	0.697	0.719	
	$L\gamma_4(L_1)$	5.181	0.068(4)	0.075	0.059	0.075	
$_{55}$Cs	$Ll(L_3)$	3.686	1.16(5)	1.11	1.12	1.14	
	$L\alpha(L_3),L\eta(L_2)$	4.283	28.0(12)	28.2	28.5	29.0	
	$L\beta_{1,3,4,6}(L_2,L_1,L_1,L_3)$	4.635	18.7(8)	18.5	18.7	18.5	
	$L\beta_{2,15,7}(L_3),L\gamma_5(L_2)$	4.934	4.64(20)	4.62	4.37	4.77	
	$L\gamma_1(L_2)$	5.275	2.48(10)	2.48	2.32	2.48	
	$L\gamma_{2,3,4}(L_1)$	5.666	1.01(5)	0.97	0.92	0.97	
$_{56}$Ba	$Ll(L_3)$	3.957	1.16(5)	1.07	1.09	1.08	1.15
	$L\alpha(L_3),L\eta(L_2)$	4.464	28.9(11)	28.1	28.4	28.4	30.3
	$L\beta_{1,6}(L_2,L_3)$	4.832	15.3(6)	14.5	14.7	14.5	16.9
	$L\beta_{2,15,7}(L_3)$	5.156	5.02(20)	4.79	4.48	4.84	5.14
	$L\gamma_{1,5}(L_2)$	5.525	2.57(12)	2.60	2.45	2.60	3.03
$_{57}$La	$Ll(L_3)$ [a]	4.123	2.17	1.12	1.14	1.21	1.08
			1.44	1.21	1.24	1.22	1.18
	$L\alpha(L_3),L\eta(L_2)$ [a]	4.649	52.4	28.8	29.0	28.8	27.8
			34.7	31.6	31.9	31.9	30.7
	$L\beta_{1,6}(L_2,L_3)$ [a]	5.046	50.9				
			33.7	15.9	16.1	15.9	16.9
	$L\beta_{2,15,7}(L_3)$ [a]	5.387	9.70	5.39	5.10	5.39	5.19
			6.43	5.55	5.23	5.60	5.39
	$L\gamma_{1,5}(L_2)$ [a]	5.787	10.4				
			6.90	2.93	2.79	2.93	3.12

[a]For the La L x rays, the experimental cross sections given in the upper row are evaluated at the Mn $K\alpha_1$ x-ray energy (5.899 keV), i.e., using $(I_0G)_{K\alpha_1}$ in Eq. (1) and those in the lower row are evaluated at the Mn $K\alpha$ x-ray energy (assuming that both the $K\alpha_1$ and $K\alpha_2$ x rays ionize the L_2 and L_3 subshells), i.e., using $(I_0G)_{K\alpha}$ in Eq. (1). Theoretical cross sections for the fluorescent transitions in $_{57}$La given in the first and second rows correspond to the Mn $K\alpha_2$ and Mn $K\alpha_1$ x-ray energy, respectively.

the tables of Scofield [38]. F_{iq} is the fractional emission rate for the Lq x rays among the radiative transitions originating from the L_i subshell. For the L x-ray emission rates, we used the rates based on the Dirac-Hartree-Slater (DHS) calculations [46] and the interpolated Dirac-Fock (DF) values by Campbell and Wang [47]. These sets differ for the $F_{1\gamma}$ and $F_{2\gamma}$ values by 5%–8% for the elements of present interest. The available data sets of the ω_i and f_{ij} values are the recently recommended values by Campbell [10] and those based on DHS calculations [9]. The ω_i ($i=1-3$) and f_{12} values [9] based on the relativistic DHS (RDHS) calculations have been recommended by Campbell [10] for the elements of present interest. The recommended values for the f_{13} and f_{23} yields [10] are lower by ~30% and ~10%, respectively,

than those based on RDHS calculations [9] and exhibit only a feeble variation in this atomic region. The sets of values σ_{Lq} (Chen-DF) and σ_{Lq} (Campbell-DF) calculated using the available data sets of ω_i and f_{ij} [9,10] and the DF x-ray emission rates [47] are listed in Table II. The calculated XRF cross sections for the elements in the present investigations are not susceptible to the CK-yield values because of their small magnitudes. Moreover, the L_i-subshell photoionization cross sections are $\sigma^P_{L_1} < \sigma^P_{L_2} < \sigma^P_{L_3}$—e.g., $\sigma^P_{L_1}:\sigma^P_{L_2}:\sigma^P_{L_3} \sim 2:3:6$—in $_{55}$Cs at the Mn $K\alpha$ x-ray energy. The sets of values, σ_{Lq} (RDHS) and σ_{Lq} (Campbell-DF) exhibit a small difference even for considerably differing f_{13} and f_{23} values. Another set σ_{Lq} (Campbell-DHS) based on the DHS emission rates [46] is also included in Table II. The σ_{Lq} (Campbell-DHS) and σ_{Lq} (Campbell-DF) values agree for the Ll, $L\alpha$, $L\beta_1$, and $L\beta_{2,15}$, x rays and differ for the $L\gamma_1$ and $L\gamma_{2,3}$ x rays. The measured values of *L* XRF cross sections in the $_{52}$Te, $_{53}$I, $_{55}$Cs, and $_{56}$Ba elements exhibit good agreement with the σ_{Lq} (Campbell-DF) and σ_{Lq} (Chen-DF). The present measurements favor DF x-ray emission rates. In the case of $_{56}$Ba, cross sections calculated using the recently measured set of the fluorescence and CK yields by Barrea *et al.* [2], σ_{Lq} (Barrea), are also included in Table II, which are in general higher than the present measured values. For deducing the measured $L\gamma_4$ XRF cross section in $_{52}$Te and $_{53}$I, the available attenuation coefficients [34] have been used in evaluation of the $m\beta$ factor [Eq. (3)]. Though the $L\gamma_4$ x-ray energy is ~7 eV below B_{L_1}, however, measured results do not evidence any significant deviation from the available attenuation coefficients due to RRS as discussed in the subsequent Sec. IV C. The measured $L\gamma_4$ XRF cross sections in $_{52}$Te and $_{53}$I agree with the $\sigma_{L\gamma 4}$ (Campbell-DF) and $\sigma_{L\gamma 4}$ (Chen-DF) values.

In view of the observed consistency in the comparison of the measured and calculated cross sections, it was thought worthwhile to deduce the ω_3 values for the$_{52}$Te, $_{53}$I, $_{55}$Cs, and $_{56}$Ba elements and the ω_2 value in case of the $_{56}$Ba element using the measured cross sections. The ω_i $(i=2,3)$ values were calculated using $\omega_i = \Sigma_q \sigma_{LqX} / \sigma^{P\tau}_{L_i}$, where the summation in the numerator is for the present measured L_i subshell $(i=2,3)$ x rays—namely, $q=\eta,\beta_1,\gamma_{1,5}$ for the L_2 subshell and $q=l,\alpha,\beta_{2,6,7,15}$ for the L_3 subshell. The intense peaks from different subshells are well separated. The contribution of the weak *L* x-ray components based on the best accepted values of parameters [Eq. (7)] were used to evaluate ω_i. The ω_3 values for $_{52}$Te, $_{53}$I, $_{55}$Cs, and $_{56}$Ba deduced in the present work are 0.080(4), 0.082(4), 0.098(5), and 0.107(5), respectively, and the ω_2 value for $_{56}$Ba is 0.108(5). These values exhibit good agreement with the RDHS values [9] recommended by Campbell [10]. Recently, Badiger and Bonzi [48] have reported widely differing measured $\omega_2 = 0.082(5)$ and $\omega_3 = 0.063(3)$ values for the $_{56}$Ba element. The ω_i and f_{ij} yields were also reported by Sögüt *et al.* [49] and Özdemir [50], but the analysis procedures involved massive corrections due to overlapping x-ray components, which in turn are based on theoretical estimation. The ratio of the L_3-subshell x-ray emission rates for $_{56}$Ba deduced from the present work is 0.176(6). It agrees with the values based on DHS [46] and DF [47] calculations, but does not support the recent value 0.226(17) [12] measured using a wavelength-dispersive setup. The fluorescence and CK yields recommended by Campbell [10] along with the DF x-ray emission rates [47] are taken as the best accepted values.

C. Resonant Raman scattering in $_{57}$La

It is clear from Figs. 2(a)–2(c) that the $L\beta_1$ x-ray (originating from L_2 subshell) peak area for the $_{52}$Te, $_{53}$I, and $_{55}$Cs elements is about half that of the $L\alpha$ x-ray (originating from L_3 subshell) peak as $\sigma^P_{L_1}:\sigma^P_{L_2}:\sigma^P_{L_3} \sim 2:3:6$ and $\omega_1:\omega_2:\omega_3 = 1:2:2$ (Table I) and also that the f_{13} CK yield is ~0.25. In the case of $_{56}$Ba, $\sigma^P_{L_1}=0$ and a similar situation persists in the spectrum shown in Fig. 2(d). In the case of $_{57}$La, the $L\beta_1$ x-ray peak is further expected to reduce by ~30%, where the L_2 subshell is ionized only by the incident Mn $K\alpha_1$ x ray. However, the $L\beta_1$ x-ray peak is observed to be significantly enhanced in the spectrum of the LaF_3 thin target [Fig. 3(a)] and is almost equal to the $L\alpha$ x-ray peak. The $L\gamma_{1,5}$ x ray is the other intense component originating from the L_2 subshell, and it overlaps with the Mn scatter peak. It is also enhanced when compared to the neighboring peak corresponding to the $L\beta_{2,15}$ x ray originating from the L_3 subshell. A similar enhancement is also observed in the spectra taken using thick pellet targets of LaF_3 [Fig. 3(b)]. The L_2- and L_3-subshell XRF cross sections were deduced using Eq. (1) with the incident photon intensity as $(I_0G)_{k\alpha_1}$ and $(I_0G)_{K\alpha}$, respectively, and ignoring contributions to the L_3-subshell vacancies due to the L_2-L_3 CK transitions. The deduced XRF cross sections are found to be significantly higher and do not fit in the trend observed for the lower-*Z* elements (Table II). If we assume that the B_{L_2} (La) is less than the Mn $K\alpha_2$ x ray energy, the deduced cross sections using the $(I_0G)_{K\alpha}$ value still deviate considerably from the observed trend (Table II). The available physical parameters hardly reproduce the observations even if we choose any of the available sets for the fluorescence and CK yields [9,10] including the recently measured one by Barrea *et al.* [39].

The $L\beta_1$ x ray originating from the L_2 subshell $(J=\frac{1}{2})$ has isotropic emission. The observed isotropy for the $L\alpha$ x rays deduced from the spectra taken at different angles [Fig. 9(c)] using the LaF_3 target and the ^{55}Fe point source also ruled out possibility of any unusual anisotropic *L* x-ray emission [14,15] or Bragg's diffraction. The target was checked for contamination from the *K* x-ray fluorescence spectra taken using high-energy γ rays from ^{241}Am [16] and ^{57}Co radioactive sources. The *L* x-ray measurements done using Cr absorbers of different thickness in conjunction with the ^{55}Fe source and also the uncovered ^{55}Fe source confirmed the observations. The LaF_3 thin targets used in the present work were procured from Micromatter on different occasions over a gap of 10 years, and a few targets were also prepared using LaF_3 procured from Indian Rare Earths Ltd., India. Similar observations were noticed using thin targets of La_2O_3 procured from Indian Rare Earths Ltd. and HIMEDIA Laboratories Pvt. Ltd., India [Fig. 3(c)]. The *L* x-ray spectra were also taken using thin targets of the $_{52}$Te, $_{53}$I, $_{55}$Cs, $_{56}$Ba, and $_{57}$La elements excited by Cu $K\alpha$ x rays from a Cu-anode x-ray tube with the Ni foil as selective absorber for the Cu

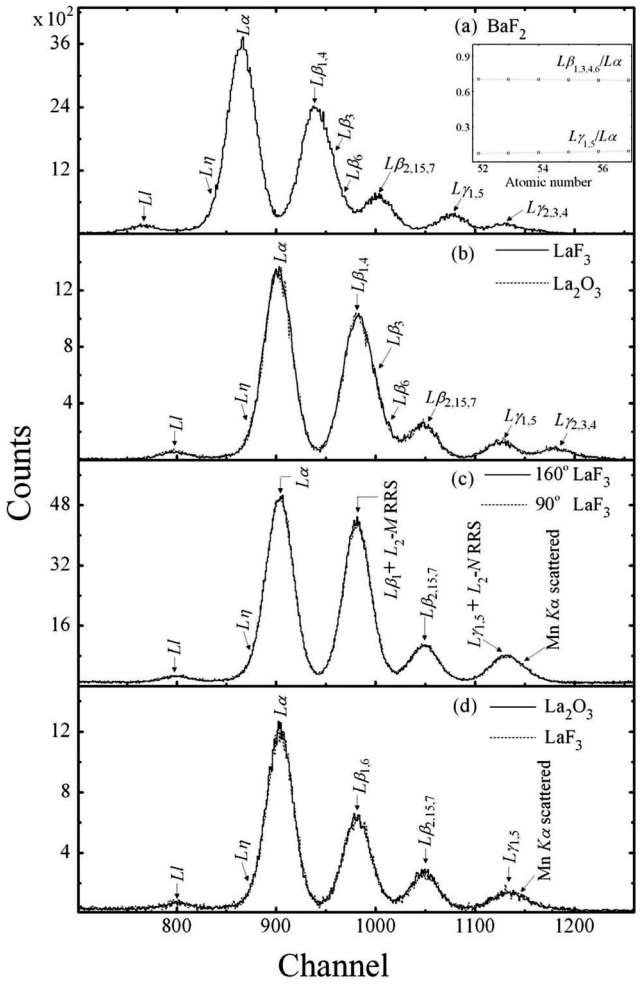

FIG. 9. (a) The $_{56}$Ba L x-ray spectrum using the BaF_2 thin target and (b) the overlapped spectra of the LaF_3 and La_2O_3 thin targets excited by the Cu $K\alpha$ x rays from the x-ray tube. (c) The overlapped spectra of the LaF_3 pellet target excited by the Mn $K\alpha$ x rays and taken at $\psi=90°$ and 160° and (d) the overlapped spectra of the LaF_3 and La_2O_3 thin targets excited by the Mn $K\alpha_1$ x ray from the ^{55}Fe source used in conjunction with a selective absorber of LaF_3 and Cr. Inset of (a) shows the intensity ratios of the L x-ray components for different elements.

$K\beta$ x ray. The x-ray spectra taken using the BaF_2, LaF_3, and La_2O_3 thin targets shown in Figs. 9(a) and 9(b) exhibit nearly the same intensity pattern. The intensity of the $L\beta_{1,3,4}$ x rays is observed to be ~70% of the $L\alpha$ x rays and remains nearly constant as a function of atomic number [inset of Fig. 9(a)], which supports the best available values of the parameters related to the photoionization and the vacancy decay processes. In the case of $_{57}$La, $\sigma_{L_1}^{P\tau}:\sigma_{L_2}^{P\tau}:\sigma_{L_3}^{P\tau}\sim 2:3:5$ at the Cu $K\alpha$ x-ray energy. The ratio of the $L\beta$ x-ray peak to the $L\alpha$ x-ray peak observed in the La target spectrum taken using Mn $K\alpha$ x rays is even higher than the value observed using Cu K x rays, despite (i) the L_1-subshell ionization by the Cu K x rays leading to additional L_3-subshell vacancies via the L_1-L_3 CK transitions and (ii) the L_2 subshell being ionized only by the Mn $K\alpha_1$ x ray and the L_3 subshell being ionized by both the Mn $K\alpha_1$ and $K\alpha_2$ x rays. The intensity ratios of the observed $L\gamma_{1,5}$ and $L\beta_1$ x rays originating from the L_2 subshell and the Ll, $L\alpha$, and $L\beta_{2,15}$ x rays from the L_3 subshell measured using $_{57}$La thin targets excited by Mn $K\alpha$ x rays do not differ significantly from the measured values using lower-Z targets. This observation strategy supports the reliability of the fractional emission rates and infers at first sight that the observed enhancement is related to the number of L_2-subshell vacancies. The extra contribution observed in the L_2-subshell x-ray peaks is construed to the L_2-subshell radiative RRS of the Mn $K\alpha_2$ x-ray component ($E_{K\alpha_2}=5.888$ keV, linewidth=1.50 eV [51]) present in the incident flux having energy below the B_{L_2} (La). For the La free atom, the values of the L_2-subshell binding energy ($B_{L_2}^{\text{atom}}$) and its level width are 5.8906 keV [36] and 3.35 eV [37], respectively. The RRS process involves excitation of an L_2-subshell core electron into an intermediate unoccupied level. This virtual state then decays by the L_2-M_4 or L_2-N_4 radiative transition and the nonradiative (Auger or L_2-L_3 CK) transitions as schematically shown in Fig. 10. In the decay of the photoexcited L_2-subshell real vacancy in $_{57}$La, the major radiative transitions are $L\beta_1$ (L_2-M_4) and $L\gamma_1$ (L_2-N_4) x rays. The major nonradiative transitions correspond to $L_2M_2M_{2,3,4,5}$ and $L_2M_4M_{4,5}$ Auger transitions, leading to double vacancies in the M shell, and $L_2L_3N_i$ ($i=1-5$) CK transitions [7]. In the RRS process, by exciting the L_2-subshell electron from the upper energy tail of the Lorentzian distribution to above the Fermi level, one scans the density of unoccupied virtual bound states in the atom. The radiative RRS profile presents a long low-energy tail (inset of Fig. 10), which is due to the Lorentzian shape of the L_2 subshell involved. The scattered energy spectrum consists of this tail, modulated with an oscillator strength distribution for the L_2-subshell absorption (dg_{L_2}/dE) and convoluted with the M_4- and N_4-subshell electron distributions. At the low-energy limit, the emitted photon energy approaches zero and the differential cross section $d\sigma/dE$ vanishes. The radiative RRS cross sections can be determined using the formulation developed by Tulkki and Åberg [23] within the Kramers-Heisenberg model. As the valence electrons are added or removed from an atom, the energy eigenvalues of the inner-shell electrons change. The formation of chemical bonding causes migration of the valence electrons among the participating atoms, thus reducing screening effects and increasing their inner-shell binding energies [28,52,53]. In a medium-heavy atom, this energy change may be of the order of a few eV and is roughly the same for the $1s$, $2p$, $3p$, and $4p$ electrons, which has been manifested as a small change of ~0.1 eV in the K-shell fluorescent x-ray energies. The La $K\alpha_1$ x-ray transition in La_2O_3 is lower by 3 meV as compared to that in the La metal [52], and the Pr $K\alpha_2$, $K\beta_1$, and $K\beta_2$ x-ray transitions observed in PrF_3 are lower by ~50 meV as compared to those in the Pr metal [52,53].

The Lorentzian distributions for the incident Mn $K\alpha_1$ and $K\alpha_2$ x rays are also shown in Fig. 10. The value of B_{L_2} (La) in LaF_3 is not known, and it is expected to be higher by the chemical shift [$(\Delta B_{L_2})\sim$few eV] as compared to $B_{L_2}^{\text{atom}}$, i.e., more toward the Mn $K\alpha_1$ x-ray centroid. If the B_{L_2} (La) in LaF_3 is about 2 eV higher than $B_{L_2}^{\text{atom}}$ and becomes equal to the minima of the sum of the Mn $K\alpha_1$ and $K\alpha_2$ x-ray distributions at 5.8926 keV, about 2% of the Mn $K\alpha_1$ x-ray dis-

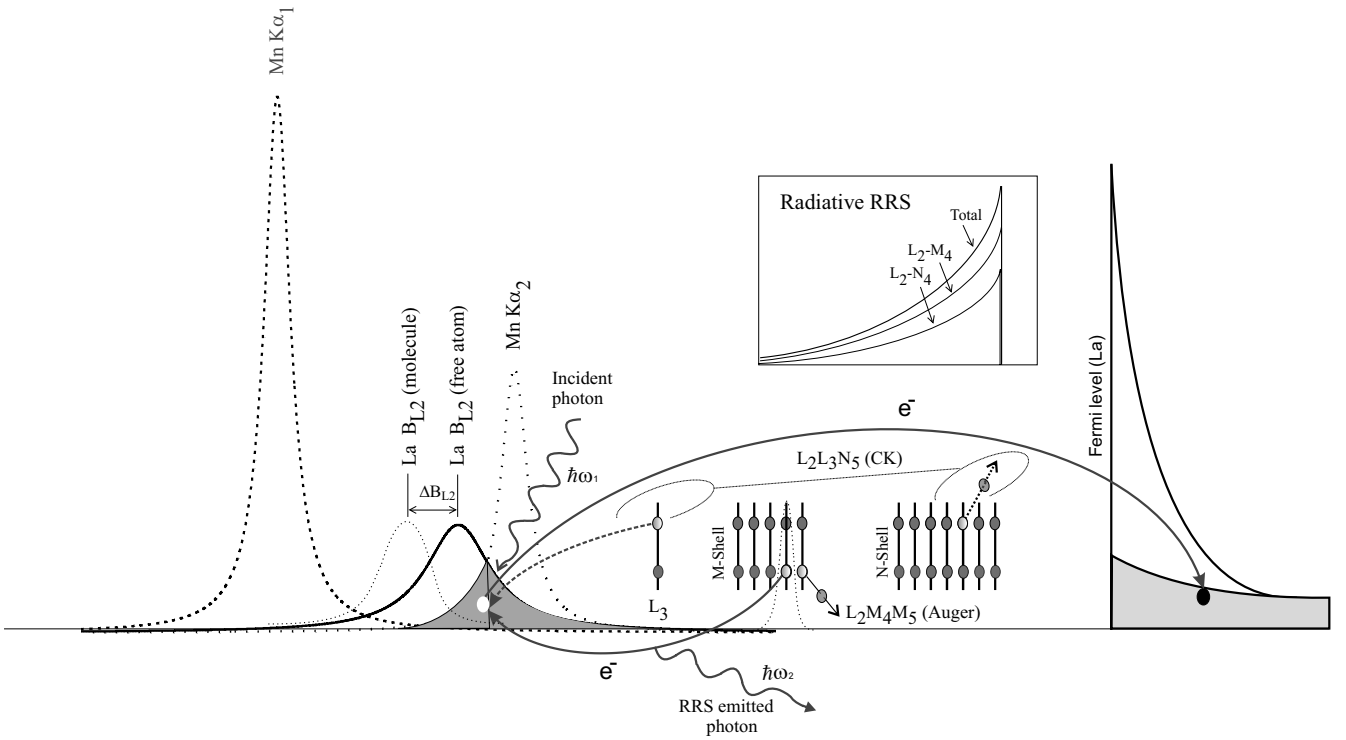

FIG. 10. The decay processes associated with the virtual vacancy produced in the L_2-subshell RRS. The Lorentzian profiles of the incident Mn $K\alpha_2$ and $K\alpha_1$ x rays and the La L_2 subshell are also shown. Inset shows the radiative RRS profiles.

tribution lies below the B_{L_2} (La) energy and is not available for photoexcitation. Similarly, about 4% of the Mn $K\alpha_2$ x-ray distribution lies above the La L_2-subshell distribution and is available for photoexcitation. The two contributions nearly cancel each other. For further analysis, we shall assume that the Mn $K\alpha_1$ and $K\alpha_2$ x-ray distributions, respectively, lie completely above and below the L_2-subshell threshold of $_{57}$La in LaF_3 and contribute to the L_2-subshell photoexcitation and RRS processes in La. The Mn $K\alpha_1$ x-ray energy lies 8.40 eV higher than $B_{L_2}^{\text{atom}}=5.8906$ keV for the La free atom.

The L XRF cross section values [Eqs. (1) and (2)] obtained using the available attenuation coefficients [34] in the case of LaF_3 thin and thick targets do not agree. To obtain the same results from the thick targets, the attenuation coefficients are required to be higher than the available values [34]. This observation further supports the RRS contribution to the fluorescent L x-ray spectrum. The available attenuation coefficients [34] do not include a RRS contribution. To corroborate the large contribution of the RRS in $_{57}$La, the total attenuation coefficient $[\mu_{K\alpha_2}^{\text{total}}(\text{La})]$ for the incident Mn $K\alpha_2$ x ray was measured for $_{57}$La in LaF_3. The measurement and evaluation procedures are given in Appendix C. The attenuation coefficient for the $_{57}$La element in the LaF_3 target is deduced to be 1122(45) cm^2/g, a value considerably higher compared to the theoretical value 486 cm^2/g for $_{57}$La at the Mn $K\alpha_2$ x-ray energy.

The peaks of the L_2-M_4 and L_2-$N_{4,1}$ radiative RRS of the Mn $K\alpha_2$ x-ray (5.888 keV) overlap with the corresponding fluorescent $L\beta_1$ and $L\gamma_{1,5}$ x-ray peaks. Although we did not perform direct measurements on RRS, we extracted the relative intensities of the radiative RRS by subtracting the contribution of the fluorescence process. The total observed area under the overlapping qth group of the L_2-subshell fluorescent x rays and the corresponding RRS peaks can be expressed as

$$N_{L_2qX+\text{RRS}} = m\varepsilon_{L_2qX+\text{RRS}}[(I_0G)_{K\alpha_1}\beta_{L_2qX}^{K\alpha_1}\sigma_{L_2qX}^{K\alpha_1} + (I_0G)_{K\alpha_2}\beta_{L_2q\text{RRS}}^{K\alpha_2}\sigma_{L_2q\text{RRS}}^{K\alpha_2}]\left(\frac{1}{4\pi}\right) + N_{\aleph}. \quad (8)$$

The first and second terms represent the fluorescent and radiative RRS contributions, respectively. $N_{\aleph}$ corresponds to the contribution of the weak L_3-subshell x rays—viz., weak $L\beta_6$ x-ray peak—which overlaps with the $L\beta_1$ x-ray and L_2-M_4 RRS peaks. Also, the $L\gamma_{1,5}$ x rays and the L_2-$N_{4,1}$ RRS peaks overlap with the Mn $K\alpha$ x-ray scatter peak. The peak-fitting procedure was used to separate the fluorescent and scatter peaks. The fitting parameters (FWHM and peak position) of the scatter peak were deduced from the spectra taken using the Te, PrF_3, and NdF_3 targets, and the same parameters were used for fitting the composite peak in the $_{57}$La spectrum [inset of Fig. 3(b)]. Consistent results for the $L\gamma_{1,5}$ x-ray intensity including RRS were obtained from the spectra taken using the thin and thick targets of LaF_3. The photopeak areas for the L_2-subshell x rays excited by the incident Mn $K\alpha_1$ x-ray components were deduced using the XRF cross sections evaluated using the best set of available parameters [Eq. (7)] and $(I_0G)_{K\alpha_1}$ value in Eq. (1). The net peak area for the L_2-M_4 and L_2-$N_{4,1}$ radiative RRS [Eq. (8)] corresponding the incident Mn $K\alpha_2$ x ray was obtained by subtracting this contribution of the fluorescent x rays and has

TABLE III. Integral L_i subshell XRF and radiative RRS cross sections (cm^2/g) and other deduced parameters in $_{57}$La.

X-ray transition	Theoretical L XRF cross section [Campbell-DF] at energy of Mn		Radiative RRS transition[a]	Radiative RRS cross sections measured using Mn $K\alpha_2$ x ray and target of		Parameter corresponding to Mn $K\alpha_2$ x ray	Value of parameter deduced using target	
	$K\alpha_1$ x ray	$K\alpha_2$ x ray		LaF_3	La_2O_3		LaF_3	La_2O_3
Ll	1.21	1.12	L_3-M_1	-	-	$\mu_{K\alpha_2}^{\text{total}}$	1122(45)	960(44)
$L\alpha$	31.6	28.8	L_3-$M_{4,5}$	11.2(16)	7.3(12)	$\mu_{K\alpha_2}^{\text{RRS}}$	636(45)	474(44)
$L\beta_1$	15.9		L_2-M_4	65.7(32)	50.2(25)	$\Sigma_q\sigma_{L_2q\text{RRS}}$(radiative)	78(4)	60(3)
$L\beta_{2,15}$	5.55	5.39	L_3-$N_{5,4}$	2.6(4)	2.2(4)	ω_2(RRS)	0.122(10)	0.126 (14)
$L\gamma_{1,5}$	2.93		L_2-$N_{4,1}$	11.5(7)	8.3(6)	f_{23}(RRS)	0.20(3)[b]	0.19[b] (3)

[a]The RRS transitions corresponding to the intense fluorescent transition are mentioned. The contribution for the weak transitions is included by using the DF fractional emission rates [47] the same as for the fluorescent transitions.
[b]Evaluated taking ω_3(RRS)=0.112 [10] the same as for the fluorescence process.

been further used to deduce the corresponding radiative RRS cross sections $\sigma_{L_2q\text{RRS}}$(radiative) at 126°.

The anisotropy in the radiative RRS was also deduced from angular distribution measurements in the range 90°–160°. The evaluation procedure is given in Appendix B. The L_2-M_4 RRS differential cross sections in the angular range 90°–160° are plotted in Fig. 8(b). The β_2 value deduced by fitting the angular-distribution polynomial is −0.002(28), which infers that the L_2-M_4 RRS is isotropic. The present result is similar to that reported for the K-shell ($J=\frac{1}{2}$) RRS by Czerwinski *et al.* [29] and Kodre and Shafroth [30]. Therefore, the L_2-subshell radiative RRS integral cross sections $\sigma_{L_2q\text{RRS}}$(radiative) were also deduced from the differential cross sections measured at 126° angle by multiplying by a factor of 4π

The total number of L_2-subshell vacancies, $\mu_{K\alpha_2}^{\text{RRS}}$(La), created in the RRS process was obtained by subtracting the theoretical value of the attenuation cross section [34] at the Mn $K\alpha_2$ x-ray energy from the present measured $\mu_{K\alpha_2}^{\text{total}}$(La) value. The available attenuation cross section values [34] include contributions of the photoionization in the L_3 subshell and higher shells and the Rayleigh and Compton scattering processes. This value is further used to calculate the fluorescence yield corresponding to the RRS process, $\omega_2(\text{RRS})=\Sigma_q\sigma_{L_2q\text{RRS}}(\text{radiative})/\mu_{K\alpha_2}^{\text{RRS}}$. The deduced ω_2(RRS) value is given in Table III.

In the case of $_{57}$La, an attempt was made to identify different contributors to the observed $L\alpha$, η, and $L\beta_{2,15}$ x-ray peaks. The $L\alpha$, η x-ray peak was corrected for ~7% contribution of the $L\eta$ x ray and the corresponding L_2-M_1 radiative RRS to deduce the $L\alpha$ x-ray peak area. The fractional rates for the radiative RRS were taken to be the same as for the fluorescent transitions. The L_3-subshell x rays measured using thick pellet targets were also corrected for additional excitation of ~3% by $L\gamma_{1,5}$ x rays and L_2-M_4 radiative RRS photons. Further, the peak areas for the $L\alpha$ and $L\beta_{2,15}$ x rays due to the incident Mn $K\alpha_1$ x ray were calculated using Eq. (1) and the XRF cross sections based on the best set of available parameters. This peak area was subtracted from the observed total peak area. The net areas were assigned to excitation by the Mn $K\alpha_2$ x ray. The deduced $L\alpha$ and $L\beta_{2,15}$ XRF cross sections were found to be higher by ~35% than the calculated values. This excess fraction was assigned to the L_3-subshell vacancies resulting from the L_2-L_3 CK transitions involving the L_2-subshell vacancies produced in the RRS process. Consistent cross section values corresponding to this extra production of the total L_3-subshell x rays were obtained from the measurements using thin and thick targets of LaF_3. Taking the liberty of using the fluorescence yield $\omega_3=0.112$ [10] to be the same for the L_3-subshell radiative RRS process, we deduced the total excess vacancies produced in the L_3 subshell corresponding to the assigned L_2-L_3 CK RRS transitions. Further using the value of the total L_2-subshell RRS cross section, $\mu_{K\alpha_2}^{\text{RRS}}$(La), a value of $f_{23}(\text{RRS})=0.20(3)$ was deduced. This value is found to be close to the value for the photoexcited L_2-subshell vacancies (Table I). The ratio of the L_2-$N_{4,1}$ and L_2-M_4 radiative RRS cross sections, 0.175(14), matches the corresponding value of 0.184 for the DF x-ray emission rates in the case of photoexcited real vacancies [47]. Also, the relative intensities of the $L\alpha$ and $L\beta_{2,15}$ x rays emitted in the decay process of the L_2-subshell vacancies produced in the RRS process agree with the DF x-ray emission rates [47].

The fluorescence measurements were also repeated using thin targets (54 and 120 $\mu g/cm^2$) and thick pellet of La_2O_3. The spectrum taken using the La_2O_3 thin target is given in Fig. 3(d) along with spectrum from the LaF_3 thin target after normalizing for the effective La mass thickness in the target. The composite peak corresponding to the L_2-M_4-subshell RRS and the $L\beta_1$ x ray from the La_2O_3 target is found to be smaller than that observed from the LaF_3 target. The deduced L_2-M_4 and L_2-$N_{4,1}$ RRS cross sections in $_{57}$La are found to be ~30% lower. For the RRS cross section evaluation in case of La_2O_3, the Mn $K\alpha_1$ and $K\alpha_2$ x-ray distributions are also assumed to lie completely above and below the B_{L_2} (La) energy. The attenuation measurements were also performed for the Mn $K\alpha$ x rays in La_2O_3 and the $\mu_{K\alpha_2}^{\text{total}}$(La) value was deduced to be 960(44) cm^2/g. The $\mu_{K\alpha_2}^{\text{total}}$(La) in La_2O_3 is found to be lower by ~15% than that deduced from LaF_3. The spectra of LaF_3 and La_2O_3 thin targets taken using the Cu-anode x-ray tube exhibit good overlap [Fig. 9(b)]. The targets were also checked for contamination from the K x-ray fluorescent spectra taken using high-energy γ rays from ^{241}Am [16] and ^{57}Co sources. The

total number of L_2-subshell vacancies, $\mu_{K\alpha_2}^{\mathrm{RRS}}(\mathrm{La})$, created in the RRS process is also obtained by subtracting the theoretical value of attenuation cross section [34] from the measured $\mu_{K\alpha_2}^{\mathrm{total}}(\mathrm{La})$ value and is found to be ~30% lower than that obtained using LaF_3 . The L_2-subshell radiative RRS cross section $\Sigma_q \sigma_{L_2 q\mathrm{RRS}}(\mathrm{radiative})$ are also lower by almost the same fraction. The fluorescence yield corresponding to the RRS process, $\omega_2(\mathrm{RRS})$, for $_{57}$La in La_2O_3 comes out to be 0.126(14), which agrees with that obtained using LaF_3 (Table III). The L_2-L_3 CK yield $f_{23}(\mathrm{RRS})$ and relative intensities of the L_2-M_4 and L_2-$N_{4,1}$ radiative RRS are also deduced and are given in Table III. These values are found to be consistent with those obtained using the LaF_3 target.

The measured value of the attenuation coefficient (1122 cm^2/g) for the Mn $K\alpha_2$ x ray in the $_{57}$La element determined using the LaF_3 absorber is higher by a factor of more than 2 as compared to the Mn $K\alpha_1$ x ray (486 cm^2/g) [34]. A photon source of Mn $K\alpha_1$ x rays was obtained using a selective absorber of LaF_3 (~4 $\mathrm{mg}/\mathrm{cm}^2$) in conjunction with an ^{55}Fe source equipped with a Cr absorber. This improved the intensity ratio of the Mn $K\alpha$ x-ray components to $I_{K\alpha_1}/I_{K\alpha_2} \sim 13$ from the value ~2 using only the Cr absorber. The spectrum taken using the LaF_3 thin target is shown in Fig. 9(d). The La L_2-subshell x-ray intensity values are found to approach the expected value. This infers the disappearance of the additional contribution due to the RRS of the Mn $K\alpha_2$ x rays. The ^{55}Fe source equipped with the LaF_3 selective absorber was also used to measure the attenuation coefficient for the Mn $K\alpha_1$ x ray in LaF_3. The deduced value of the attenuation coefficient 502 cm^2/g is close to the theoretical value of 486 cm^2/g [34] corresponding to the Mn $K\alpha_1$ x ray. Similar observations were made regarding the fluorescent x-ray spectrum [Fig. 9(d)] and the measured attenuation coefficient in the case of $_{57}$La using the La_2O_3 absorber.

In the analysis of the data taken using the LaF_3 and La_2O_3 targets, we took that the Mn $K\alpha_1$ and $K\alpha_2$ x-ray distributions lie completely above and below the B_{L_2} (La) energy and the results obtained are reasonably consistent. However, the value of the binding energy B_{L_2} (La) is not known in these La compounds. The sharp high-energy cutoff in the RRS spectrum is defined by the energy conservation and moves linearly toward lower energies with a decrease in the incoming photon energy (inset of Fig. 10). More specifically, if ΔB_{L_2} is the perturbation in the B_{L_2} binding energy due to chemical bonding, the maximum RRS energy from an atom bound in a molecule will be equal to $E_{\mathrm{in}}-(B_{L_2}+\Delta B_{L_2})$. The shift to a lower maximum scattered energy will also result in a decrease in the total RRS intensity, since a slice from the RRS distribution with width equal to ΔB_{L_2} will not be available. Using the wavelength-dispersive equipment, both the energy shift and intensity change can be manifested in the form of spectrum shape, i.e., $d^2\sigma/d\Omega dE$ [24]. However, using the energy-dispersive semiconductor detector the information mainly regarding the integral RRS cross sections is obtained. It is difficult to observe changes in the line shape or energy shift using a semiconductor detector [28]. Solid-state detectors with advances in signal processing techniques [54] can be useful for such kinds of studies. The electrons in the lower tail below the incident photon energy contribute to RRS and, a shift in the binding energy is responsible for the observed difference in the L_2-subshell RRS cross sections. In this simple picture, the integral RRS cross sections were evaluated by taking the product of the slice from the Mn $K\alpha_2$ intensity profile and the number of electrons in the La L_2-subshell distribution below the slice energy. It is estimated that the binding energy of the L_2 subshell in $_{57}$La in LaF_3 needs to be lower by ~1 eV than that in La_2O_3 to account for the observed ~30% difference in the RRS cross sections.

Further, we explored the variation of the deduced values of parameters—viz., the radiative RRS cross sections and total attenuation coefficients including RRS ($\mu_{K\alpha_2}^{\mathrm{total}}$) in $_{57}$La as a function of chemical shift (ΔB_{L_2}), i.e., the difference in the L_2-subshell binding energy for the $_{57}$La element in the chemical molecule and the free atom. For analysis of the measured data using the LaF_3 and La_2O_3 compounds, the $I_o G_{K\alpha_1}$ and $I_o G_{K\alpha_2}$ values used in Eqs. (8) and (C1) were taken as the relative intensities of the exciting photons available for the RRS and fluorescence processes, respectively—i.e., the $K\alpha$ x-ray photons having energy below and above the B_{L_2} (La), respectively. These values were deduced from the Mn $K\alpha_1$ and $K\alpha_2$ x-ray distributions (Fig. 10) for different values of chemical shift, ΔB_{L_2}, in the range 0–8 eV. Total attenuation coefficients ($\mu_{K\alpha_2}^{\mathrm{total}}$) including the RRS contributions and the total RRS contributions ($\mu_{K\alpha_2}^{\mathrm{RRS}}$) for the Mn $K\alpha_2$ x-ray and the radiative $[\omega_2(\mathrm{RRS})]$ and CK $[f_{23}(\mathrm{RRS})]$ yields corresponding to the L_2-subshell RRS process in $_{57}$La were evaluated for different values of ΔB_{L_2} and are plotted in Figs. 11(a) and 11(b), respectively. The radiative RRS cross sections decrease slowly as expected because of an increase in the number of photons below B_{L_2}. The values of ω_2 (RRS) and f_{23} (RRS) exhibit relatively slower variations as a function of ΔB_{L_2}. It is interesting noting that the ω_2 (RRS) and f_{23} (RRS) yields in $_{57}$La are consistent with the values corresponding to decay of the photoexcited real vacancies [Figs. 11(a) and 11(b)].

The $_{57}$La element has ground-state electronic configuration $[\mathrm{Xe}]5d^1 6s^2$ with an unoccupied state of $5d$ orbit and the $4f$ and $6p$ states fully unoccupied. It has electronegativity 1.1 on the Pauling scale. In lanthanum (III) fluoride and dilanthanum (III) trioxide, chemical bonding of $_{57}$La will influence its atomic energy levels and the inner-shell electronic transitions. The electronegativity of $_9$F with electronic configuration $[\mathrm{He}]2s^2 2p^5$ is 3.98 on the Pauling scale, which is greater than the value of 3.40 in the case of $_8$O having electronic configuration $[\mathrm{He}]2s^2 2p^4$. The bonding in the case of LaF_3 is more ionic in character than in La_2O_3. Keeping in mind the more polymeric nature of the La_2O_3 structure and ionic character of LaF_3, one expects higher binding energy for the L_2-subshell electron in the free molecule of LaF_3 as compared to that in La_2O_3. The RRS integral cross sections based on the simple picture (Fig. 10) should be lower in the case of a LaF_3 free molecule than that of La_2O_3. The present contrary observations are possibly related to the band structure in LaF_3 and La_2O_3 solid compounds. LaF_3 is an optically transparent solid with a hexagonal lattice and a band gap of ~10.3 eV [55]. La_2O_3 is also well known for its high

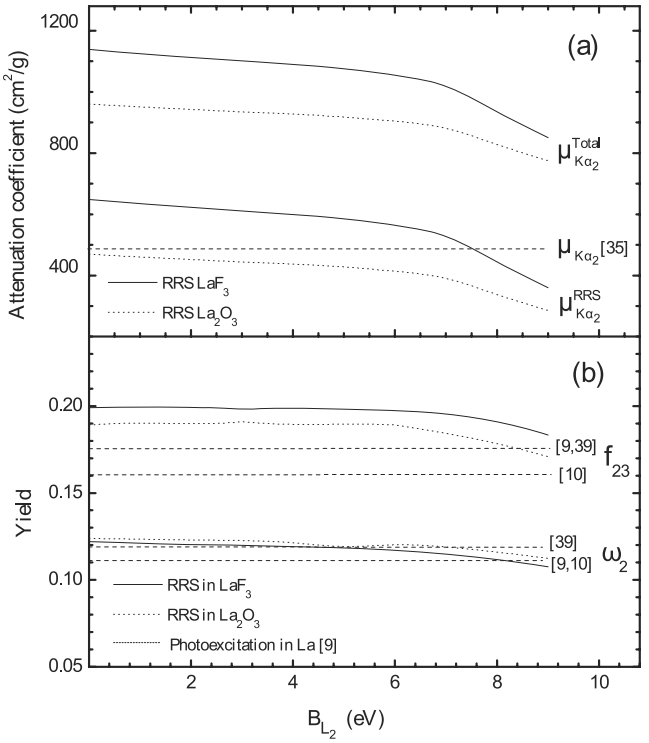

FIG. 11. (a) Total attenuation coefficients ($\mu_{K\alpha_2}^{\text{total}}$), including RRS and excluding RRS ($\mu_{K\alpha_2}$) [34] contributions, and total RRS contributions ($\mu_{K\alpha_2}^{\text{RRS}}$) for the Mn $K\alpha_2$ x ray in $_{57}$La using the LaF_3 and La_2O_3 chemical compounds and (b) the radiative [ω_2(RRS)] and CK [f_{23}(RRS)] yields corresponding to the L_2 subshell RRS process in $_{57}$La as a function of the difference in the L_2-subshell binding energy (ΔB_{L_2}) of $_{57}$La in free-atom form from that in chemical-molecule form. Horizontal dashed lines in (b) correspond to ω_2 and f_{23} values for the vacancies produced by photoexcitation.

dielectric constant with a band gap of 4.3 eV [56]. Nakai *et al.* [25] investigated the resonant emission spectra across the $_{39}$Y L_3-absorption threshold in Y-metal and Y-insulator compounds—namely, YF_3, YCl_3, and Y_2O_3. The electronic configuration of $_{39}$Y is [Kr] $4d^15s^2$ and is similar to that of $_{57}$La. In the Y-insulator compounds, a Raman-scattering component consisting of a two-peak structure, the main and subpeaks differing in energy by a few eV, has been observed at incident photon energies below the L_3-absorption threshold. The intensities of the Raman peaks are resonantly enhanced as the incident photon energy reaches the absorption edge. Above the absorption threshold, both Raman and normal $L\alpha$ emission peaks have been observed in insulator samples. At the increasing incident photon energies above the absorption edge, the intensity of the Raman peak decreases and it disappears at about 20 eV above the absorption peak. On the other hand, in Y metal, only the normal $L\alpha$ emission peak has been observed above the absorption threshold. In YF_3, YCl_3 and Y_2O_3 compounds, the observed intensity of the subpeaks relative to the Raman peak decreases in this order. This has been explained from the calculations of Mizouchi [35], which showed the strong dependence of the subpeak intensity on the band structure of the compound. Mizouchi [35] theoretically discussed relaxation of the core-electron excitation processes and explained the radiative RRS, characteristic x-ray, and absorption spectra in wide-gap insulators by taking a four-band model composed of dispersionless deep and shallow core bands and valence and conduction bands. The present radiative RRS measurements in case of La wide-gap insulator compounds using limited resolution of the semiconductor detector cannot visualize the fine peak structure similar to that observed in Y compounds by Nakai *et al.* [25]. The present work is based on broadband RRS involving Mn $K\alpha$ x rays. In the case of the LaF_3 and La_2O_3 insulator compounds, the portion of the Mn $K\alpha$ x rays, especially the $K\alpha_1$ x ray, lies higher by less than 8.40 eV depending upon the value of chemical shift (ΔB_{L_2}). The additional contribution to the Raman peak due to the Mn $K\alpha_1$ x ray photons above the B_{L_2} (La) energy, and in the form of Raman subpeaks in LaF_3 due to the Mn $K\alpha_2$ x-ray photons having energy below the B_{L_2} (La) energy is expected to be higher than in La_2O_3. In order to understand these mechanisms, one needs further experiments for La compounds using the wavelength-dispersive setup and tunable synchrotron source. It will also be interesting to measure the La compounds in dissolved form, i.e., by destroying the valence and conduction bands in the solid-state crystal structure.

V. CONCLUSION

We studied the decay of L_i ($i=1-3$) subshell vacancies in $_{52}$Te, $_{53}$I, $_{55}$Cs, $_{56}$Ba, and $_{57}$La elements excited by Mn $K\alpha_1$ and $K\alpha_2$ x rays through measurements of radiative emission using a modest-resolution energy-dispersive x-ray setup. The parameters related to decay of the L_i-subshell real and virtual vacancies produced in the fluorescence and RRS processes, respectively, have been investigated. The fluorescence yields recommended by Campbell [10] and the DF x-ray emission rates [47] form the best available set of L_i-subshell vacancy decay parameters. The present measurements are not susceptible to the CK yields. The incident photon energy should be well above the L_1-subshell binding energy for measurements of the CK yields, where photoionization in the L_1 and L_2 subshells is dominant [3], and it should be close to the L_i-subshell binding energies for measurements of the L_i-subshell fluorescence yields. It is found that the L_2-subshell radiative RRS in $_{57}$La corresponding to the Mn $K\alpha$ x rays accounts for the observed higher L_2-subshell x-ray intensity. The radiative decay of the L_3-subshell vacancies produced in intrashell transfer via the L_2-L_3 CK RRS transition also leads to enhancement in the L_3-subshell x-ray intensity. The RRS and the total attenuation cross sections measured in $_{57}$La using LaF_3 and La_2O_3 targets are found to differ significantly, which is contrary to the trend expected on the basis of the chemical state of the $_{57}$La element. The unexpected observed difference in the LaF_3- and La_2O_3-insulator compounds is likely to be related to the contribution of processes explained on the basis of the four-band model of Mizouchi [35] involving participation of valence and conduction bands along with the inner subshells. Parameters like fractional emission rates, fluorescence yield, and CK yield associated with decay of the L_2-subshell RRS process are also found to be consistent with those associated

with decay of the photoexcited real vacancies in $_{57}$La. Further measurements are needed at incident photon energies tuned across the La L_2-subshell threshold in a variety of La compounds using synchrotron sources and wavelength-dispersive and energy-dispersive detection setups. It is further suggested that the existing database used in various softwares [57] needs to be updated in light of the RRS contributions. The angular dependences of the L_2-subshell RRS and the L_3-subshell $L\alpha_{1,2}$ and $L\beta_{2,15}$ fluorescent x-ray emission have been measured to be nearly isotropic. However, small anisotropy is indicated in pure Ll x-ray emission though within experimental error and its magnitude is of the order of the theoretical prediction. More efforts are required to improve the experimental error.

The $_{57}$La element and Mn $K\alpha_2$ x-ray combination is one of the best target-radioisotope combinations for investigating the RRS process. The La L_2-subshell RRS has been observed with intensities comparative to fluorescent x rays using a less-cumbersome and handy ^{55}Fe radioactive source. The RRS can be explored for *in vivo* investigations of different physical and chemical forms involving $_{57}$La whose chemical compounds, especially at nanosizes, are gaining applications in industry as well as in research laboratories [55,56]. It certainly requires precise calibration of the Lorentzian distributions associated with Mn $K\alpha_1$ and $K\alpha_2$ x rays using a wavelength-dispersive setup. The ^{55}Fe radioactive source along with La and Cr selective absorbers for the Mn $K\alpha_2$ and $K\beta$ x rays, respectively, offers a monochromatic source of Mn $K\alpha_1$ x rays.

ACKNOWLEDGMENTS

Financial support from the Department of Science and Technology (DST), New Delhi, under FIST and the University Grants Commission (UGC), New Delhi, under the Centre of Advance Study in Physics is gratefully acknowledged. V.S. and S.K. acknowledge financial support from the DST, New Delhi, and the Council of Scientific and Industrial Research (CSIR).

APPENDIX A: EFFECT OF GEOMETRICAL ANGULAR SPREAD ON THE EFFECTIVE THICKNESS OF THE TARGET

As the photon energies involved in the measurements are low, it is necessary to verify the effect of angular spread on the effective thickness of the target ($m\beta$) in the present annular source geometrical setup (Fig. 1). The computer simulations [27,40] were exercised to determine the number of L x-ray photons, $\tilde{N}(\theta_i, \theta_e)$, reaching the detector for different θ_i and θ_e angles. The $\tilde{N}(\theta_i, \theta_e)$ distribution was corrected for absorption in the Cr absorber and self-absorption in the source. The effective thickness values $m\beta_{Lq}(\theta_i, \theta_e)$ were calculated using Eq. (3) for different θ_i and θ_e angles [Fig. 5(c)], and their average value $(m\beta_{Lq})_{\text{avg}}$ was calculated with $\tilde{N}(\theta_i, \theta_e)$ as the weighing factor. This average value differs by 0.5% from that calculated using the same distribution of θ_i but taking $\theta_e = 0°$. The distribution of number of incident photons, $\tilde{N}(\theta_i)$, as a function of the effective thickness $m\beta(\theta_i, \theta_e)$ for the present geometrical setup is shown in Fig. 5(d). Also, a difference of ~0.5% was noticed in $(m\beta_{Lq})_{\text{avg}}$ due to a change in the distribution by using a 10-mg/cm^2 Mylar absorber with ^{55}Fe source. Both these corrections were applied to the $m\beta$ value for the thick targets calculated using Eq. (3) by taking the measured effective incident angle $\theta_i = 126°$ and the emission angle $\theta_e = 0°$. The corrected $m\beta$ values were used in Eq. (1). For the angular distribution setup [Fig. 4(b)], similar simulations were also exercised for evaluation of effective thickness ($m\beta$) of the target [40].

APPENDIX B: EVALUATION OF THE ANISOTROPY PARAMETER FOR FLUORESCENT X RAYS AND RRS IN $_{57}$La

In the case of $_{57}$La, the anisotropy for the $L\alpha$ and $L\beta_{2,15}$ fluorescent x rays was inferred from the measured photopeak area N_{L_3qX}, which also includes a small contribution due to the L_2-subshell RRS via the L_2-L_3 CK decay (Sec. IV C). The differential cross sections were evaluated at different angles using the expression

$$\left[\frac{d\sigma}{d\Omega}(\psi)\right]_{L_3qX}^{K\alpha_1} = \frac{N_{L_3qX}}{m\beta_{L_3qX}^{K\alpha_1}\tau(I_0G)_{K\alpha_1}\varepsilon_{L_3qX}[1+\mathfrak{I}]}, \quad \text{(B1)}$$

where

$$\mathfrak{I} = \left[\beta_{L_3qX}^{K\alpha_2}(I_0G)_{K\alpha_2}\left(\frac{d\sigma}{d\Omega}(\psi)\right)_{L_3qX}^{K\alpha_2}\right] \Big/ \left[\beta_{L_3qX}^{K\alpha_1}(I_0G)_{K\alpha_1}\left(\frac{d\sigma}{d\Omega}(\psi)\right)_{L_3qX}^{K\alpha_1}\right].$$

The differential cross section ratio

$$\left[\frac{d\sigma}{d\Omega}(\psi)\right]_{L_3qX}^{K\alpha_2} \Big/ \left[\frac{d\sigma}{d\Omega}(\psi)\right]_{L_3qX}^{K\alpha_1}$$

is angle independent. The Mn $K\alpha_1$ and $K\alpha_2$ x-ray energies are well above B_{L_3}; therefore, the anisotropy for the L_3q x ray at both excitation energies is expected to be same [44].

For the Ll x-ray emission in $_{57}$La, where separate measurements were performed without the CaF_2 reference target, the anisotropy is deduced relative to that of the $L\alpha$ x ray. Again taking the ratio

$$\left[\frac{d\sigma}{d\Omega}(\psi)\right]_{Ll}^{K\alpha_2} \Big/ \left[\frac{d\sigma}{d\Omega}(\psi)\right]_{Ll}^{K\alpha_1}$$

to be angle independent, the ratio of differential cross sections for the Ll and $L\alpha$ x rays can be expressed as

$$\frac{\left[\frac{d\sigma}{d\Omega}(\psi)\right]_{Ll}^{K\alpha_1}}{\left[\frac{d\sigma}{d\Omega}(\psi)\right]_{L\alpha}^{K\alpha_1}} = \frac{N_{Ll}}{N_{L\alpha}} \frac{\beta_{L\alpha}^{K\alpha_1}}{\beta_{Ll}^{K\alpha_1}} \frac{[1+\chi(\beta_{L\alpha}^{K\alpha_2}/\beta_{L\alpha}^{K\alpha_1})]}{[1+\chi(\beta_{Ll}^{K\alpha_2}/\beta_{Ll}^{K\alpha_1})]}, \quad \text{(B2)}$$

where χ includes terms that remain constant for the measurements at different emission angles.

The angular distribution data for the L_2-subshell RRS in $_{57}$La were also analyzed. The L_2-M_4 radiative RRS peak of the Mn $K\alpha_2$ x ray overlaps with the peak corresponding to the $L\beta_1$ x ray [originating from the L_2 subshell $(J=\frac{1}{2})$] resulting from excitation by the Mn $K\alpha_1$ x ray. The emission of the $L\beta_1$ x ray is isotropic. The differential cross sections for the L_2-M_4 radiative RRS at different emission angles were deduced by subtracting the isotropic contribution of the $L\beta_1$ x ray from the observed composite peak area, $N_{L\beta_1+L_2q\mathrm{RRS}}$—i.e., using the expression

$$\left[\frac{d\sigma}{d\Omega}(\psi)\right]_{L_2\mathrm{RRS}}^{K\alpha_2} = \frac{N_{L\beta_1+L_2q\mathrm{RRS}} - [m_s\beta_{L\beta_1}^{K\alpha_1}\tau\varepsilon_{L\beta_1}(I_0G)_{K\alpha_1}\sigma_{L\beta_1}^{K\alpha_1}]}{m_s\beta_{L\beta_1}^{K\alpha_2}\tau\varepsilon_{L\beta_1}(I_0G)_{K\alpha_2}}, \quad \text{(B3)}$$

where various symbols have the same meaning as mentioned earlier and τ is the attenuation correction for incident Mn $K\alpha$ x rays in the CaF_2 reference target. The second term constitutes about half of the first term and has only a feeble angular dependence as similar terms appear in the denominator.

APPENDIX C: MEASUREMENTS OF ATTENUATION COEFFICIENTS

The total attenuation coefficient $[\mu_{K\alpha_2}^{\mathrm{total}}(\mathrm{La})]$ for the incident Mn $K\alpha_2$ x ray was measured for $_{57}$La in LaF_3 using the geometrical setup shown in Fig. 4(c). The Mn $K\alpha_1$ and $K\alpha_2$ x-ray peaks cannot be resolved using the LEGe detector and $\mu_{K\alpha_2}^{\mathrm{total}}(\mathrm{La})$ was deduced from the measured fraction of the total transmitted intensity, $N(K\alpha)/N_o(K\alpha)$, for the $K\alpha$ x rays through LaF_3 absorbers of different thickness ≤ 1 mg/cm^2. For a LaF_3 absorber of thickness m, the expression for $\mu_{K\alpha_2}^{\mathrm{total}}(\mathrm{La})$ is

$$\mu_{K\alpha_2}^{\mathrm{total}}(\mathrm{La}) = -\left(\frac{1}{m}\right)\log_e\left[\frac{I_{K\alpha_1}}{I_{K\alpha_2}}\left\{\left(\frac{N(K\alpha)}{N_0(K\alpha)}\right)_{\mathrm{obs}}\left(1+\frac{I_{K\alpha_2}}{I_{K\alpha_1}}\right) - \exp(-m\mu_{K\alpha_1})\right\}\right](w_{\mathrm{La}}+w_F) - w_F\mu_F, \quad \text{(C1)}$$

where ω_{La} and ω_{F} are the weight fractions for the La and F elements in the target, $I_{K\alpha_1}/I_{K\alpha_2}$ is the intensity ratio of the Mn $K\alpha_1$ and $K\alpha_2$ x rays, and a value of 1.9712 was used after correction for absorption in the source. It is worth mentioning that a change of 5% in the $I_{K\alpha_1}/I_{K\alpha_2}$ ratio results in a 1.4% change in the deduced $\mu_{K\alpha_2}^{\mathrm{total}}(\mathrm{La})$ value. The transmission of the Mn $K\alpha$ x rays, $N(K\alpha)/N_0$, was measured in the LaF_3 absorber with Mylar backing. The measurements were performed using the Mn $K\alpha$ and $K\beta$ x rays measured simultaneously from the ^{55}Fe source. The absorption of the Mn $K\beta$ x ray was used to verify the thickness of the LaF_3 absorber. The transmitted intensity for the $K\alpha$ x ray was used in Eq. (C1) to deduce $\mu_{K\alpha_2}^{\mathrm{total}}(\mathrm{La})$ for LaF_3. A second set of measurements were performed using the Mn and Fe $K\alpha$ x rays from the ^{55}Fe and ^{57}Co radioactive sources, respectively. The emitted $K\beta$ x rays were selectively absorbed in the Cr and Mn absorbers used with ^{55}Fe and ^{57}Co radioactive sources. The transmission for the Fe $K\alpha$ x rays from the ^{57}Co source were also measured to verify the LaF_3 absorber thickness. The procedure involves sequential measurements for (i) the intensity of the Mn $K\alpha$ x rays from the ^{55}Fe source with equivalent of Mylar backing at the absorber position, (ii) the intensity for the Mn $K\alpha$ x rays with the LaF_3 absorber on Mylar backing, (iii) the intensity for the Fe $K\alpha$ x rays from the ^{57}Co radioactive source without disturbing the LaF_3 absorber, and (iv) the intensity for the Fe $K\alpha$ x rays with equivalent of Mylar backing at the absorber position. The attenuation coefficients deduced for the LaF_3 at the Mn $K\alpha_2$ x ray using the two procedures are found to agree within 5%. The Mn $K\beta$ and Fe $K\alpha$ x-ray energies are well above the La L_1 subshell threshold and the tabulated attenuation coefficients [34] are expected to be reliable.

[1] U. Werner and W. Jitschin, Phys. Rev. A **38**, 4009 (1988).
[2] R. A. Barrea, C. A. Pérez, and H. J. Sánchez, Nucl. Instrum. Methods Phys. Res. B **215**, 308 (2004) and references therein.
[3] M. Sharma, P. Singh, S. Puri, D. Mehta, and N. Singh, Phys. Rev. A **69**, 032501 (2004) and references therein.
[4] W. Jitschin, in *X-ray and Inner-shell Processes*, edited by T. Carlson, O. Krause, and T. Monson, AIP Conf. Proc. No. 215 (AIP, New York, 1990), p. 408.
[5] P. V. Rao, Pramana J. Phys. **50**, 669 (1998).
[6] M. O. Krause, J. Phys. Chem. Ref. Data **8**, 307 (1979).
[7] M. H. Chen, B. Crasemann, and H. Mark, At. Data Nucl. Data Tables **24**, 13 (1979).
[8] J. H. Hubbell, P. N. Trehan, N. Singh, B. Chand, D. Mehta, M. L. Garg, R. R. Garg, S. Singh, and S. Puri, J. Phys. Chem. Ref. Data **23**, 339 (1994).
[9] S. Puri, D. Mehta, B. Chand, N. Singh, and P. N. Trehan, X-Ray Spectrom. **22**, 358 (1993).
[10] J. L. Campbell, At. Data Nucl. Data Tables **85**, 291 (2003).
[11] R. D. Bonetto, A. C. Carreras, J. Trincavelli, and G. Castellano, J. Phys. B **37**, 1477 (2004).
[12] Y. Zou, M. Oura, R. Hutton, H. Yamaoka, N. Takeshima, K. Takahiro, K. Kawatsura, and T. Mukoyama, J. Phys. B **39**,

4775 (2006).
[13] S. Flügge, W. Mehlhorn, and V. Schmidt, Phys. Rev. Lett. **29**, 7 (1972).
[14] J. K. Sharma and K. L. Allawadhi, J. Phys. B **32**, 2343 (1999).
[15] S. Seven, Radiat. Phys. Chem. **69**, 451 (2004).
[16] D. Mehta, S. Puri, N. Singh, M. L. Garg, and P. N. Trehan, Phys. Rev. A **59**, 2723 (1999).
[17] T. Papp and J. L. Campbell, J. Phys. B **25**, 3765 (1992).
[18] H. Yamaoka, M. Oura, K. Takahiro, T. Morikawa, S. Ito, M. Mizumaki, S. Semenov, N. Cherepkov, N. Kabachnik, and T. Mukoyama, J. Phys. B **36**, 3889 (2003).
[19] H. Küst, U. Kleiman, and W. Mehlhorn, J. Phys. B **36**, 2073 (2003).
[20] R. A. Barrea, C. A. Pérez, T. S. Plivelic, E. V. Bonzi, and H. J. Sánchez, J. Phys. B **38**, 839 (2005).
[21] C. J. Sparks and G. E. Ice, Indian J. Phys., B **71B**, 393 (1997).
[22] S. Manninen, Radiat. Phys. Chem. **50**, 77 (1997).
[23] J. Tulkki and T. Åberg, J. Phys. B **15**, L435 (1982).
[24] J. Szlachetko, J.-Cl. Dousse, M. Berset, K. Fennane, M. Szlachetko, J. Hoszowska, R. Barrett, M. Pajek, and A. Kubala-Kukus, Phys. Rev. A **75**, 022512 (2007); Nucl. Instrum. Methods Phys. Res. B **238**, 353 (2005).
[25] S. Nakai, Y. Megawa, F. Terasaki, Gang Chen, T. Ohuchi, K. Obara, T. Kojima, H. Arai, T. Kashiwakura, and Y. Kitajima, Phys. Rev. B **61**, 7433 (2000).
[26] H. J. Sánchez, M. C. Valentinuzzi, and C. A. Pérez, J. Phys. B **39**, 4317 (2006).
[27] S. Kumar, V. Sharma, D. Mehta, and N. Singh, Nucl. Instrum. Methods Phys. Res. B **264**, 1 (2007).
[28] A. G. Karydas, S. Galanopoulos, Ch. Zarkadas, T. Paradellis, and N. Kallithrakas-Kontos, J. Phys.: Condens. Matter **14**, 12367 (2002) and references therein.
[29] H. Czerwinski, F. Smend, D. Schaupp, M. Schumacher, A. H. Millhouse, and H. Schenck-Strauss, Z. Phys. A **322**, 183 (1985).
[30] A. F. Kodre and S. M. Shafroth, Phys. Rev. A **19**, 675 (1979).
[31] G. S. Brown, M. H. Chen, B. Crasemann, and G. E. Ice, Phys. Rev. Lett. **45**, 1937 (1980).
[32] Y. Baba, T. A. Sasaki, and H. Yamamoto, Phys. Rev. B **49**, 709 (1994).
[33] K. Ichikawa, O. Aita, K. Aoki, M. Kamada, and K. Tsutsumi, Phys. Rev. B **45**, 3221 (1992).
[34] M. J. Berger and J. H. Hubbel, computer code XCOM, version 3.1, National Bureau of Standards, Gaithersburg, MD, USA, 1999, available from http://physics.nist.gov/.
[35] H. Mizouchi, Phys. Rev. B **58**, 15557 (1998).
[36] E. Browne and R. B. Firestone, in *Table of Radioactive Isotopes*, edited by V. S. Shirley (Wiley, New York, 1986).
[37] J. L. Campbell and T. Papp, At. Data Nucl. Data Tables **77**, 1 (2001).
[38] J. H. Scofield (unpublished).
[39] R. A. Barrea, C. A. Pérez, and H. J. Sánchez, Spectrochim. Acta B **58**, 51 (2003).
[40] S. Kumar, V. Sharma, D. Mehta, and N. Singh, Phys. Rev. A **77**, 032510 (2008).
[41] J. Singh, R. Singh, D. Mehta, N. Singh, and P. N. Trehan, in *Proceedings of the DAE Symposium on Nuclear Physics*, edited by R. K. Choudhury and A. K. Mohanty [Nucl. Phys. B **37**, 455 (1995)].
[42] O. Mauron, J.-Cl. Dousse, S. Baechler, M. Berset, Y.-P. Maillard, P.-A. Raboud, and J. Hoszowska, Phys. Rev. A **67**, 032506 (2003).
[43] S. Puri, B. Chand, D. Mehta, M. L. Garg, N. Singh, and P. N. Trehan, At. Data Nucl. Data Tables **61**, 289 (1995).
[44] E. G. Berezhko, N. M. Kabachnik, and V. S. Rostovsky, J. Phys. B **11**, 1749 (1978).
[45] E. G. Berezhko and N. M. Kabachnik, J. Phys. B **10**, 2467 (1977).
[46] J. H. Scofield, At. Data Nucl. Data Tables **14**, 121 (1974).
[47] J. L. Campbell and J. X. Wang, At. Data Nucl. Data Tables **43**, 281 (1989).
[48] N. M. Badiger and E. V. Bonzi, Nucl. Instrum. Methods Phys. Res. B **243**, 34 (2006).
[49] Ö. Söğüt, E. Büyükkasap, and M. Ertuğrul, X-Ray Spectrom. **30**, 427 (2001).
[50] Y. Özdemir, Radiat. Phys. Chem. **66**, 317 (2003).
[51] A. A. Markowicz, in *Handbook of X-ray Spectrometry*, edited by R. E. van Grieken and A. A. Markowicz (Marcel Dekker, New York, 2002), Vol. 14, p. 53.
[52] F. Boehm, in *Atomic Inner-shell Processes*, edited by B. Crasemann (Academic press, New York, 1975), Vol. 1, p. 433.
[53] P. L. Lee, F. Boehm, and P. Vogel, Phys. Rev. A **9**, 614 (1974).
[54] T. Papp, J. L. Campbell, and E. Papp-Szabó, Nucl. Instrum. Methods Phys. Res. B **189**, 33 (2002).
[55] A. S. El-Said, R. Neumann, K. Schwartz, and C. Trautmann, Surf. Coat. Technol. **158-159**, 522 (2002).
[56] Y. Gao, Y. Masuda, and K. Koumoto, J. Colloid Interface Sci. **274**, 392 (2004).
[57] J. A. Maxwell, W. J. Teesdale, and J. L. Campbell, Nucl. Instrum. Methods Phys. Res. B **95**, 407 (1995).